The Astrophysical Journal, 905:40 (15pp), 2020 December 10 https://doi.org/10.3847/1538-4357/abc7c4


# The Rapid Buildup of Massive Early-type Galaxies: Supersolar Metallicity, High Velocity Dispersion, and Young Age for an Early-type Galaxy at $z = 3.35$

Paolo Saracco[1], Danilo Marchesini[2], Francesco La Barbera[3], Adriana Gargiulo[4], Marianna Annunziatella[5], Ben Forrest[6], Daniel J. Lange Vagle[2], Z. Cemile Marsan[7], Adam Muzzin[7], Mauro Stefanon[8], and Gillian Wilson[6]
[1] INAF—Osservatorio Astronomico di Brera, via Brera 28, I-20121 Milano, Italy; paolo.saracco@inaf.it
[2] Tufts University, Physics and Astronomy Department, 574 Boston Ave., Medford, MA 02155, USA
[3] INAF—Osservatorio Astronomico di Capodimonte, sal. Moiariello 16, I-80131 Napoli, Italy
[4] INAF—Istituto di Astrofisica e Fisica Cosmica, IASF, via A. Corti 12, I-20133 Milano, Italy
[5] Centro de Astrobiologia (CSIC-INTA), Spain (PI)
[6] Department of Physics and Astronomy, University of California, Riverside, CA 92521, USA
[7] Department of Physics and Astronomy, York University, Toronto, ON M3J 1P3, Canada
[8] Leiden Observatory, Leiden University, Leiden, The Netherlands
*Received 2020 July 20; revised 2020 November 2; accepted 2020 November 3; published 2020 December 10*

## Abstract

How massive early-type galaxies (ETGs) assembled their mass, on which timescales the star formation quenched, and when their supersolar metallicity has been established are still open and debated issues. Thanks to very deep spectroscopic observations carried out at the Large Binocular Telescope, we simultaneously measured stellar age, metallicity, and velocity dispersion for C1-23152, an ETG at redshift $z = 3.352$, corresponding to an epoch when the universe was ∼1.8 Gyr old. The analysis of its spectrum shows that this galaxy, hosting an active galactic nucleus (AGN), formed and assembled $\sim 2 \times 10^{11}\ M_{\odot}$, shaping its morphology within the ∼600 Myr preceding the observations, since $z \sim 4.6$. The stellar population has a mean mass-weighted age of $400^{+30}_{-70}$ Myr, and it is formed between ∼600 and ∼150 Myr before the observed epoch, the latter being the time since quenching. Its high stellar velocity dispersion, $\sigma_e = 409 \pm 60$ km s$^{-1}$, confirms the high mass ($M_{\rm dyn} = 2.2\ (\pm 0.4) \times 10^{11}\ M_{\odot}$) and the high mass density ($\Sigma_e^{M^*} = \Sigma_{\rm 1kpc} = 3.2\ (\pm 0.7) \times 10^{10}\ M_{\odot}$ kpc$^{-2}$), suggesting a fast dissipative process at its origin. The analysis points toward a supersolar metallicity, $[{\rm Z/H}] = 0.25^{+0.006}_{-0.10}$, in agreement with the above picture, suggesting a star formation efficiency much higher than the replenishment time. However, subsolar-metallicity values cannot be firmly ruled out by our analysis. Quenching must have been extremely efficient to reduce the star formation to SFR $< 6.5\ M_{\odot}$ yr$^{-1}$ in less than 150 Myr. This could be explained by the presence of the AGN, even if a causal relation cannot be established from the data. C1-23152 has the same stellar and physical properties of the densest ETGs in the local universe of comparable mass, suggesting that they are C1-23152-like galaxies that evolved to $z = 0$ unperturbed.

*Unified Astronomy Thesaurus concepts:* Galaxy formation (595); Galaxy evolution (594); High-redshift galaxies (734); Elliptical galaxies (456); Galaxy stellar content (621); Galaxy properties (615)

## 1. Introduction

In the classical paradigm of hierarchical galaxy formation, high-mass early-type galaxies (ETGs) grow their stellar mass mainly ex situ through subsequent mergers of smaller preexisting galaxies over timescales comparable to the Hubble time (e.g., De Lucia et al. 2006). In seeming contrast, studies of local ETGs show that they follow tight scaling relations between stellar population properties (age and metallicity) and physical properties (stellar velocity dispersion, mass, and size), whose tightness is not consistent with a predominant merging process (Nipoti et al. 2012) but requires a short star formation event (e.g., Renzini 2006). These studies also suggest that the larger the mass of a galaxy, the higher the redshift at which most of its stars formed and the shorter the duration of star formation (Thomas et al. 2010). Some simulations suggest that an early intense burst of star formation followed by a rapid quenching is required to reproduce the structural properties of ETGs and to match the tight scaling relations (e.g., Ciotti et al. 2007; Naab et al. 2007; Oser et al. 2012; Brooks & Christensen 2016).

Local studies also show that the larger the mass of a galaxy, the higher the stellar metallicity and the older the stars (e.g., Gallazzi et al. 2006). This is rather counterintuitive since older stellar populations are expected with lower metallicity than younger ones. However, these properties result from the integrated effect of galaxy evolution across the whole Hubble time, making it difficult to disentangle evolutionary from formation processes. Since stellar metallicity is most sensitive to the efficiency of gas replenishment during star formation and to the quenching mechanism (e.g., Peng et al. 2015; Maiolino & Mannucci 2019), the measurement of stellar metallicity in massive ETGs at high redshift would provide important information on these two fundamental processes of galaxy formation.

In the past decade, deep and wide photometric surveys have discovered massive ($M^* > 10^{11}\ M_{\odot}$) quiescent galaxies at $z > 2$–3, i.e., formed during the first 2–3 Gyr of cosmic time (e.g., Marchesini et al. 2010; Cassata et al. 2013; Straatman et al. 2014). Spectroscopic observations have confirmed the high-redshift nature for some of them, establishing the presence of passive galaxies at $2 < z < 3$ with ages comparable to the age of the universe at that redshift (e.g., Cimatti et al. 2008; Kriek et al. 2009; Gobat et al. 2012; van de Sande et al. 2013; Belli et al. 2014, 2017).

More recently, spectroscopic observations have confirmed the presence of massive passive galaxies at $z > 3$ (Marsan et al. 2015; Glazebrook et al. 2017; Schreiber et al. 2018;

Tanaka et al. 2019, 2020; D'Eugenio et al. 2020; Forrest et al. 2020a; Valentino et al. 2020, Forrest et al. 2020b). The importance of pushing in the search for passive massive galaxies to higher redshift is due to the constraints on models of galaxy formation coming from the short cosmic time at the disposal of galaxies to assemble their stellar mass. Indeed, the latest generation of galaxy formation models, e.g., Illustris (Wellons et al. 2015) and TNG300 (Springel et al. 2018), has difficulty in reproducing these galaxies since, at $z > 3$, there is little time (<2 Gyr) for smaller progenitors to build up their stellar mass, halt star formation, and completely merge (Forrest et al. 2020a).

For some of these massive passive galaxies, the age of their stellar populations has been constrained through a parametric fitting of their spectra and broadband photometry, showing a large range in their ages (Glazebrook et al. 2017; Schreiber et al. 2018; Tanaka et al. 2019; Forrest et al. 2020a; Valentino et al. 2020; Forrest et al. 2020b). So far, it has been possible to measure the stellar velocity dispersion for only one of these objects, dynamically confirming the high mass of the system (Tanaka et al. 2019).

While these massive passive galaxies at high redshift seem to have already completed their assembly, nothing is known about their stellar metallicity. The unknown stellar metallicity does not allow for constraining either the timescale of the star formation or the possible quenching mechanisms, both affecting stellar metallicity differently (e.g., Peng et al. 2015). Additionally, the uncertainty in measured stellar ages for some of them does not allow for precise estimates of their assembly time and the duration of the quenching process. How ETGs have accreted their stellar mass, whether in situ through a main star formation event in <1 Gyr (e.g., Thomas et al. 2010) or rather ex situ through mergers in >2–3 Gyr (e.g., Boylan-Kolchin et al. 2008), or even through both processes at different times in a two-phase formation scenario (Oser et al. 2010; Hill et al. 2017; Newman et al. 2018), is still an open and debated issue.

We have simultaneously measured stellar age, metallicity, and velocity dispersion for C1-23152, a galaxy at $z = 3.352$ (Marsan et al. 2015), when the universe was less than 2 Gyr old, with very deep (17 hr of integration) spectroscopic observations carried out at the Large Binocular Telescope (LBT). In this paper we present the analysis and results. The paper is organized as follows. In Section 2 we summarize the properties of C1-23152 and describe the comparison data for ETGs at redshift $z \sim 0$. In Section 3 we describe the observations and the data reduction. In Section 4 we present the spectrum and analyze its properties. In Section 5 we derive the stellar age and metallicity and constrain the star formation history (SFH); we also derive the stellar mass and measure stellar velocity dispersion. In Section 6 we discuss the results and present our conclusions.

Throughout, we use the cosmological parameters $H_0 = 70$ km s$^{-1}$ Mpc$^{-1}$, $\Omega_\Lambda = 0.7$, and $\Omega_M = 0.3$. Magnitudes are given in the AB photometric system. All the radii presented in the paper are circularized. A Chabrier (2003) initial mass function (IMF) is assumed throughout this paper.

## 2. Data and Models

### 2.1. Galaxy C1-23152 at z = 3.35

Galaxy C1-23152 (R.A. = $10^h00^m27^s.81$, decl. = $+02^d33^m49^s.3$; J2000) was first presented in Marchesini et al. (2010) in a photometric study of a stellar mass complete sample of galaxies at $3 < z < 4$ using the NEWFIRM Medium-Band Survey. C1-23152 was then spectroscopically confirmed by Marsan et al. (2015) to be at $z = 3.352$ using a combination of Keck-NIRSPEC, VLT-Xshooter, and GTC-Osiris spectra. The SED modeling on the combined spectra and broad-/medium-band photometry resulted in an ongoing star formation rate (SFR) <7 $M_\odot$ yr$^{-1}$ and negligible dust extinction (Marsan et al. 2015). From the analysis of the emission lines and the infrared SED, C1-23152 was found to harbor a powerful type 2 quasar (QSO), with bolometric luminosity of $\sim 10^{46}$ erg s$^{-1}$, only mildly contaminating the stellar emission, with a lower limit to the stellar mass of $1.9 \times 10^{11}$ $M_\odot$ (as taken from Marsan et al. 2015 after scaling to Chabrier IMF). Structural properties were derived from the analysis of Hubble Space Telescope (HST) ACS F814W and WFC F160W images, resulting in an effective radius $R_e \simeq 1$ kpc and a Sérsic index $n \simeq 4.4$ in F160W (Marsan et al. 2015).

### 2.2. Local Comparison Samples

As comparison samples of local ETGs the following data have been considered: a sample of ETGs selected from SPIDER (La Barbera et al. 2010) with $\sigma_e > 150$ km s$^{-1}$ to represent the whole population irrespective of their mass and size; the sample of ETGs with $\sigma_e > 350$ km s$^{-1}$ studied by Bernardi et al. (2006), representing the most massive ETGs in the local universe; the sample of compact ETGs with high velocity dispersion studied by Saulder et al. (2015), representing ETGs with high mass density and extreme structural and dynamical properties; and the sample of compact galaxies identified by Damjanov et al. (2015), representing the population of small, compact, and dense galaxies missed by the current ground-based surveys.

### 2.3. Stellar Population Models

In this analysis, we adopted the EMILES simple stellar population (SSP) models (Vazdekis et al. 2015), based on BaSTI isochrones (Pietrinferni et al. 2004) and Galaxy abundance ratios ([Fe/H] = [Z/H]) as a reference library, assuming a Chabrier (2003) stellar IMF, with ages spanning [0.06; 2.0] Gyr, and 11 metallicity [Z/H] in the range [−2.32; 0.26] (a total of 162 SSPs). Notice that models with [Z/H] = 0.4, although available, were not used in the analysis, as they have lower quality than the other models (see Vazdekis et al. 2015, for details). We also considered a set of MILES $\alpha$-enhanced models (Vazdekis et al. 2015) for which [$\alpha$/Fe] = 0.4, spanning the same ranges of ages and metallicity of the reference set. In the optical spectral range, these models have an FWHM spectral resolution of 2.5 Å (Beifiori et al. 2011), higher than the rest-frame resolution (~3 Å) of the LBT-LUCI spectrum of C1-23152.

The dependence of the stellar population properties on the adopted models was tested by considering also BC03 SSPs (Bruzual & Charlot 2003) with a Chabrier IMF, including 20 ages in the range [0.06; 2.0] Gyr and five metallicities in the range [−1.7; 0.4], and Maraston & Strömbäck (2011) MILES-based models (M11) with a Chabrier IMF, including 20 ages in the range [0.06; 2.0] Gyr and five metallicities in the range [−2.3; 0.3] (see Section 5).

## 3. Spectroscopic Observations and Data Reduction

Long-slit spectroscopy of galaxy C1-23152 was obtained at the Large Binocular Telescope (LBT) with the two LBT Utility Cameras in the Infrared (LUCI1 and LUCI2; Ageorges et al. 2010) in twin (binocular) configuration, for a total effective integration time of 17.3 hr. Observations were carried out on 2018 January and 2019 January, with a seeing FWHM = 0.″8–1.″0 (in the visual), with filter HK coupled with the grism G200 sampling the wavelength range 15000–23500 Å covering the rest-frame range 3450 Å $< \lambda_{\rm rest} <$ 5300 Å at the redshift of the galaxy, at 4.35 Å pixel$^{-1}$. We adopted a slit width of 0.″75, resulting in a spectral resolution $R \simeq 1267$ (1650) in H (K) ($\Delta\lambda \sim 13$ Å for both the bands). Observations consisted of a sequence of exposures of 300 s each taken at dithered (ABBA) positions offset by ∼5″, summing up to 203 images. A bright pivot star (U0900.06569623; R.A. = 0:00:32.39, decl. = +02:34:07.08; $K_{\rm Vega} = 13.14$ mag, spectral type M) 71″ away from the target galaxy was included in the slit to ensure accurate slit centering and alignment of dithered sequences, as well as to check the flux calibration and the correction for telluric absorption lines in the data reduction phase.

The 2D spectra were processed at the Italian LBT Spectroscopic Reduction Center with a reduction pipeline optimized for LBT data (Scodeggio et al. 2005; Magrini et al. 2012). For each one of the two observing runs (2018 January and 2019 January), calibration frames were created for both LUCI1 and LUCI2. A bad pixel map was generated from flats and darks, while a "master" dark and a "master" flat were created averaging a set of darks and spectroscopic flats, respectively. Each spectral image was independently corrected for cosmic rays and bad pixels, and then dark and flat-field corrections were applied.

For the wavelength calibration, an inverse solution of the dispersion was created for each observing day and for each spectrograph. The mean accuracy reached at the center of the H and K bands is 0.5 Å (rms). For each frame, the slit was extracted and wavelength calibrated, removing any curvature due to the optical distortions.

Subtraction of emission from the sky was performed following the method developed by Davies (2007) on the 2D-extracted and wavelength-calibrated spectra. Further sky residuals along the spatial direction were removed by fitting and subtracting the signal for each column of the spectrum.

Particular attention was paid to the relative flux calibration since it can affect the shape of the spectrum. For each observing day, a sensitivity function, as well as telluric absorption correction, was obtained for LUCI1 and LUCI2 using a telluric star observed close in time and air mass to the scientific target. The wavelength/flux-calibrated and sky-subtracted spectra obtained in the different nights were finally stacked together. Offsets between different frames were estimated using the pivot stars in the science exposures.

In Figure 1, the final LBT-LUCI 1D spectrum of the pivot star U0900.06569623 (gray curve) is compared with the spectrum of the main-sequence M1 spectroscopic standard star HD 42581 (green curve).[9] The reliability of the continuum shape is a fundamental issue in the analysis of a galaxy spectrum since its shape depends on the age and metallicity of the underlying stellar population and on the dust extinction.

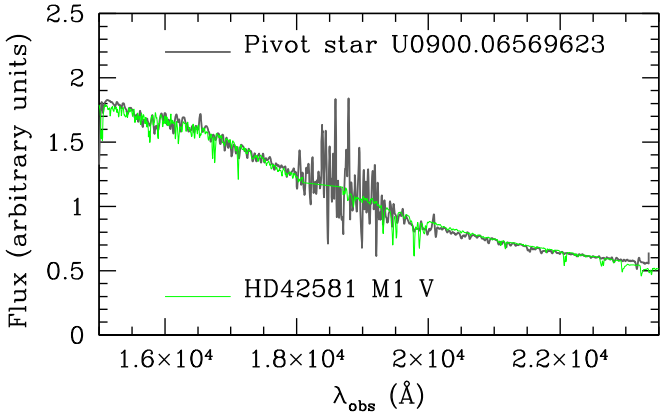


**Figure 1.** Final LBT-LUCI 1D spectrum of the pivot star U0900.06569623 smoothed over 4 pixels (∼17 Å; gray curve) compared with the spectrum of the main-sequence M-type star HD 42581 (green curve). The two spectra have been normalized to the mean flux measured in the wavelength range 1.7–1.8 $\mu$m. The comparison shows the perfect recovery of the true shape of the spectrum thanks to the careful correction for the response function of the instrument.

This comparison shows a very good agreement, demonstrating the excellent recovery of the true shape of the continuum and, therefore, the excellent quality of the relative flux calibration for the C1-23152 spectrum.

In order to extract the 1D spectrum of the galaxy, we first removed the residual background component due to the bright star observed in the scientific exposures. This component was accurately removed by running the IRAF task `background` on the two-dimensional stacked spectrum. The center of the 2D galaxy spectrum was accurately modeled by fitting the profile along the spatial direction with a double Gaussian function, in wavelength bins, excluding pixels contaminated by sky residuals/telluric absorption, in each bin. The one-dimensional (1D) spectrum of the galaxy was extracted within a region of ±3 pixels (0.″75) around the photometric center of the galaxy. We adopted an extraction radius of 3 pixels, as this turned out to maximize the signal-to-noise ratio (S/N) of the extracted spectrum.

## 4. The Spectrum of C1-23152

The 1D LBT-LUCI spectrum of C1-23152 is shown in the middle panel of Figure 2. The top panel shows the atmospheric transmission in the wavelength range of observations. The bottom panel shows, for comparison, the spectrum of a post-starburst galaxy in the local universe selected from the Sloan Digital Sky Survey (SDSS). The spectrum of C1-23152 has an S/N ≃ 3 Å$^{-1}$ around 4000 Å, and it is characterized by prominent emission lines and absorption features.

### *4.1. Emission Lines: Active Galactic Nucleus and Star Formation*

The spectrum shows strong [OII] ($\lambda$3727) and [OIII] ($\lambda\lambda$4958, 5007) doublet emission lines and weak H$\beta$ emission. The measured fluxes associated with these lines are $F_{\rm OII} = 4.0\ (\pm0.5) \times 10^{-17}$ erg cm$^{-2}$ s$^{-1}$, $F_{\rm OIII} = 1.3\ (\pm0.3) \times 10^{-16}$ erg cm$^{-2}$ s$^{-1}$, and $F_{\rm H\beta} = 4.3\ (\pm2) \times 10^{-18}$ erg cm$^{-2}$ s$^{-1}$, respectively.[10] The high luminosity of the [OIII]

[9] The spectrum has been taken from the NASA Infrared Telescope Facility (IRTF) spectral library http://irtfweb.ifa.hawaii.edu/~spex/IRTF_Spectral_Library/.

[10] Fluxes were estimated by fitting a Gaussian function to the line after having removed the underlying continuum evaluated through a polynomial fitting of the regions adjacent to the line.

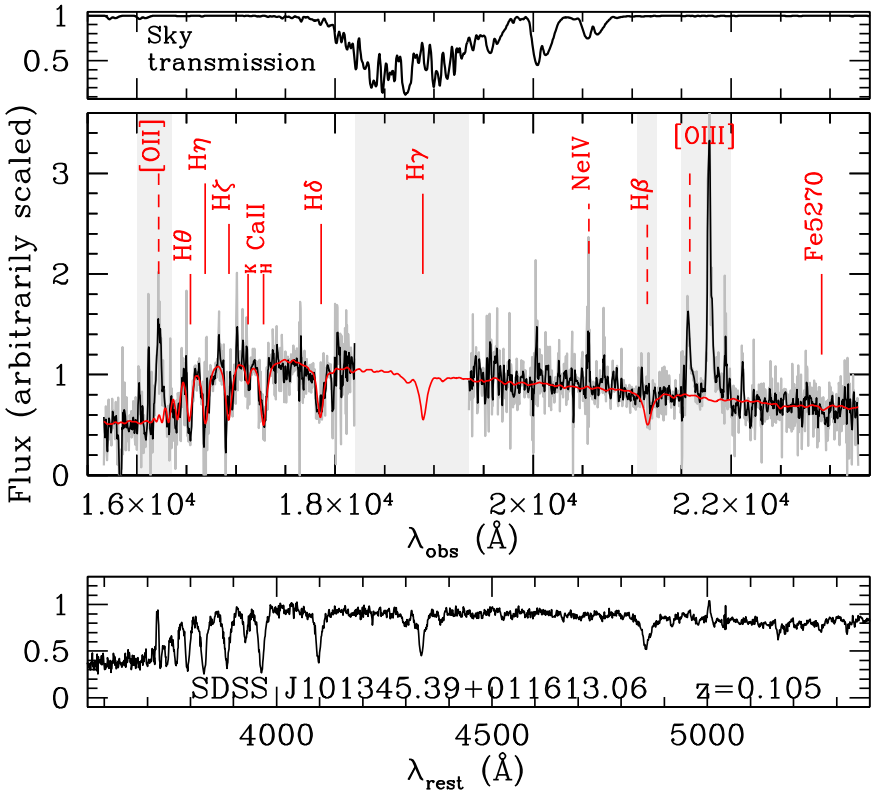


**Figure 2.** Spectrum of galaxy C1-23152. The top panel shows the atmospheric transmission in the wavelength range of observations. In the middle panel the one-dimensional spectrum of galaxy C1-23152 is shown in the original form (dark-gray curve, 4.35 Å pixel$^{-1}$, S/N $\simeq$ 3 Å$^{-1}$) and smoothed by a boxcar filter over 3 pixels (black curve) corresponding to the instrumental resolution ($\Delta\lambda \simeq 13$ Å FWHM). The main absorption and emission lines are marked by solid and dashed lines, respectively. The red curve is the best-fitting composite model obtained with STARLIGHT (see Section 5). The shaded gray regions are those masked in the fitting because of bad sky transmission or the presence of emission lines. For comparison, the bottom panel shows the observed spectrum of a typical post-starburst galaxy in the local universe selected from the SDSS.

($\lambda$5007) line, $L_{\rm OIII} = 1.3(\pm0.3) \times 10^{43}$ erg s$^{-1}$ derived from the measured flux, cannot be produced by star formation and suggests the presence of an active galactic nucleus (AGN; Francis et al. 1991). This is also confirmed by the high value of the ratios [OIII]/H$_\beta \simeq 30$ and [OIII]/[OII] $> 3$, with both of them in the AGN regime (Baldwin et al. 1981), and by the detailed study of the infrared spectral energy distribution (SED) presented by Marsan et al. (2015).

The presence of an AGN makes it difficult to estimate the possible ongoing star formation from the detected emission lines.[11] To circumvent this problem, we derived an upper limit to the current residual SFR assuming that all the H$\beta$ emission is due to star formation. To this end, we corrected the measured flux for the expected H$\beta$ absorption ($F_{\rm abs} = 6.7 \times 10^{-19}$ erg cm$^{-2}$ s$^{-1}$) according to the best-fitting composite model (see Section 5.1), assuming no dust extinction. We obtained $F_{\rm H\beta,corr} = 5.0\ (\pm2.0) \times 10^{-18}$ erg cm$^{-2}$ s$^{-1}$. Using the relation $L_{\rm H\alpha} = 2.86 L_{\rm H\beta}$ for case B recombination (Moustakas et al. 2005), we obtained $L_{\rm H\alpha} = 1.4\ (\pm0.6) \times 10^{42}$ erg s$^{-1}$. The corresponding upper limit to the SFR is 6.6 ($\pm$3.0) $M_\odot$ yr$^{-1}$, where we used the relation (scaled to Chabrier IMF) SFR $= 4.65 \times 10^{-42} L_{\rm H\alpha}$ (Kennicutt 1998b). This upper limit agrees well with the one derived from the fitting to the whole SED by Marsan et al. (2015) (see above).

### 4.2. Absorption Lines: Age-sensitive Features

The spectrum clearly shows the hydrogen Balmer absorption lines H$\theta$, H$\eta$, H$\zeta$, and H$\delta$, along with CaII (H and K), extremely weak Mg $b$, and Fe ($\lambda$5270). Table 1 summarizes the measured spectral indices (first row) and their errors at 1$\sigma$ (second row).

The Balmer lines are typical of the post-starburst phase since they are associated with hot, high-mass (1.5–2 $M_\odot$), rapidly evolving stars whose main-sequence lifetimes are less than 800 Myr (e.g., Poggianti & Barbaro 1997). Their strengths are related to the elapsed time since the end of the last burst of star formation, i.e., the time since quenching. Figure 3 (left panel) shows the expected H$\delta_A$ index for an SSP (EMILES models) seen at different ages for three different values of stellar metallicity (colored curves). The figure shows that the strength measured for galaxy C1-23152, H$\delta_A = 7.7 \pm 0.8$ Å (black solid line), defines two possible quenching epochs, at $<$200 Myr and at $\sim$600–800 Myr, for solar or supersolar metallicity.

The right panel of Figure 3 shows, instead, the expected amplitude of the D4000 index (Bruzual 1983). This discontinuity is produced by the opacity of the stellar atmospheres that, in turn, depends on the ionized metals and hence on the stellar temperature. Hot stars, responsible for H$\delta$, do not contribute to the amplitude of D4000 since their elements are multiply ionized and their opacity is low. Therefore, the D4000 index,

[11] Using the [OII] emission, considering the relation [OII]/[OIII] = 0.21 (Silverman et al. 2009), we obtained an average AGN contribution $L({\rm OII})_{\rm AGN} = 2.7\ (\pm0.2) \times 10^{42}$ erg s$^{-1}$. Therefore, the contribution of the star formation to [OII] emission is $L({\rm OII})_{\rm SF} = 1.3\ (\pm0.2) \times 10^{42}$ erg s$^{-1}$, which, using the relation (scaled to Chabrier IMF) SFR $= 8.2 \times 10^{-42} L_{\rm OII}$ (Kennicutt 1998b), provides SFR $= 10\ M_\odot$ yr$^{-1}$.

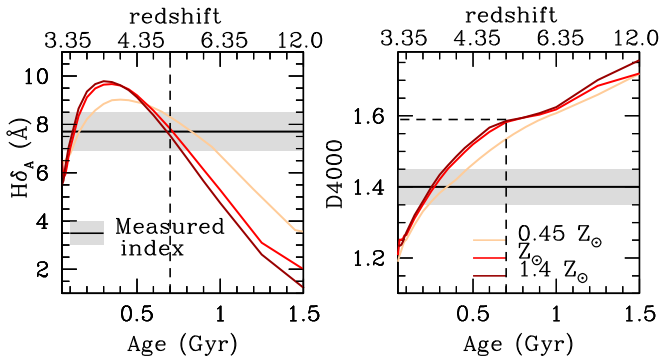


**Figure 3.** Strength of the spectral indices H$\delta_A$ (left) and D4000 (right) expected for three stellar populations of different metallicity (solid curves; orange curve, 0.45 $Z_\odot$; red curve, $Z_\odot$; and brown curve, 1.4 $Z_\odot$) as a function of age. Curves were obtained using EMILES SSPs (Vazdekis et al. 2015). The black line represents the strength of the indices measured for C1-23152 (see Table 1); the gray shaded region represents the error at 68% confidence level. The black dashed line marks the value that the two indices would have if quenching would have taken place 700 Myr prior to observations, one of the two possible epochs suggested by the H$\delta_A$ index (left).

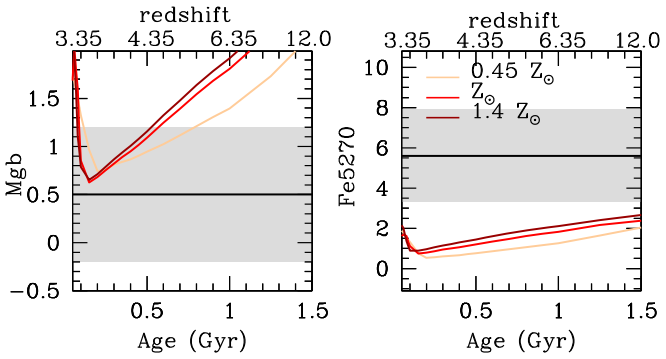


**Figure 4.** Strength of the spectral indices Mg $b$ ($\lambda$5175) (left) and Fe ($\lambda$5270) (right) expected for a stellar population with different metallicity seen at different ages (colored curves) and measured for galaxy C1-23152 (black line). Symbols are as in Figure 3.

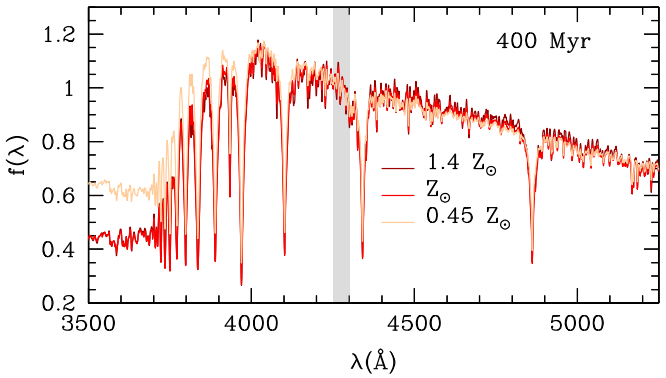


**Figure 5.** Colored curves represent three EMILES SSPs 400 Myr old for three metallicity values, 0.45 $Z_\odot$ (orange), $Z_\odot$ (red), and 1.4 $Z_\odot$ (dark red). The gray region marks the interval 4250–4300 Å where the SSPs are normalized.

contrary to H$\delta$, is dominated by low-mass stars, and hence its amplitude is strictly related to the age of the bulk of the stellar population. The measured D4000 $= 1.40 \pm 0.05$ (black solid line, right panel of Figure 3) suggests a mean age for the stellar population in the range of 250–450 Myr. This mean age rules out the solution for quenching to be 600–800 Myr before observations (which would require D4000 $> 1.6$, black dashed line, $>3\sigma$ in excess of the measured value) and constrains the bulk of the star formation to occur within the past $<$700 Myr. Combined with the H$\delta_A$ measurement, the time since quenching is restricted to $<$200 Myr. We verify these conclusions following a more careful and detailed analysis in Section 5.

### *4.3. Absorption Lines: Metallicity-sensitive Features*

Three main metal lines fall in the LUCI spectrum of C1-23152: CN3883, Mg $b$ ($\lambda$5175), and Fe ($\lambda$5270), all of them having low S/N (see Table 1). The coincidence of the Fe ($\lambda$5270) feature with a strong sky emission line makes the measured strength of this feature rather uncertain.

Figure 4 shows the line strength of Mg $b$ ($\lambda$5175) (left) and Fe ($\lambda$5270) (right) for EMILES SSPs with three different metallicities (see colored curves) as a function of age. The horizontal black lines are the line strengths as measured for C1-23152. These indices are widely used to derive stellar metallicity and abundances. Models show that the two features are extremely weak and, as expected, weakly dependent on metallicity at young ages ($\leqslant$500 Myr). Namely, for metallicity in the range 0.45–1.4 $Z_\odot$, the maximum variation of Mg $b$ is less than 10% for ages younger than 500 Myr and $<$30% at 700 Myr. A similar behavior is seen for Fe ($\lambda$5270), with the difference that for ages older than 500 Myr the maximum variation is nearly constant, by about 25%. The weak sensitivity of these indices to variations in metallicity at young ages is model independent, as we verified considering BC03 (Bruzual & Charlot 2003) and Maraston & Strömbäck (2011) (M11) models. Therefore, given the young mean age of the stellar population, these indices are not expected to provide significant constraints on stellar metallicity.

Figure 5 shows the spectra of three SSPs of different metallicity at fixed age, 400 Myr, in the wavelength range 3500–5200 Å. These models show that absorption features at shorter wavelengths and the continuum shape around D4000 are more dependent on metallicity, contrary to the features at longer wavelengths. Therefore, at young ages, Balmer lines, D4000, and continuum shape can constrain stellar metallicity more than metal lines. We will take advantage of this in the next section, being certain of the reliability of the continuum shape of our spectra (see Section 3 and Figure 1).

## 5. Analysis

In this section we describe the analysis performed to estimate the stellar age, metallicity, and velocity dispersion of C1-23152. The aim is to constrain the formation timescale of this ETG, i.e., the time needed to fully assemble and shape this galaxy as seen at $z = 3.35$, and the mechanism of mass growth, i.e., whether the stellar mass of this galaxy was assembled in situ through star formation or ex situ through accretion.

### *5.1. Age and Metallicity Estimates*

Stellar age and metallicity were derived through two different methods: absorption-line fitting (ALF) and full spectral fitting (FSF).

*ALF.*—We performed ALF (La Barbera et al. 2013; Saracco et al. 2019) by comparing the measured line strengths with those predicted by SSP models of varying age and metallicity.

**Table 1**
Measured Spectral Indices for C1-23152

| CN3883[a] | Hθ [b] | Hη [b] | Hζ [b] | Hϵ [b] | CaII (HK)[c] | D4000[d] | $D_n$ [e] | $H\delta_A$ [f] | $H\delta_F$ [f] | Mg $b$[f] | Fe5270[f] |
|---|---|---|---|---|---|---|---|---|---|---|---|
| −0.07 | 5.8 | 7.8 | 9.9 | 8.4 | 7.0 | 1.40 | 1.09 | 7.7 | 5.5 | 0.5 | 5.6 |
| (0.04) | (1.0) | (1.3) | (1.1) | (0.9) | (1.6) | (0.05) | (0.06) | (0.8) | (0.9) | (0.8) | (2.3) |

**Notes.** Indices are corrected for galaxy velocity dispersion. The correction was derived by comparing the indices measured on the best-fitting model smoothed to the $\sigma_{obs}$ of the galaxy and those of the same model at the nominal resolution of the spectral library.
[a] As defined in Davidge & Clark (1994).
[b] Defined ad hoc in this work to avoid as much as possible sky residuals in the pseudocontinuum regions.
[c] As defined by Serven et al. (2005).
[d] As defined by Bruzual (1983).
[e] As defined by Balogh et al. (1999).
[f] As defined by Worthey & Ottaviani (1997) and Trager et al. (1998). Note that the coincidence with a strong sky emission line makes the measured strength of Fe5270 rather unreliable. For this reason, this feature was not considered in the absorption-line fitting.

The fitting was performed by minimizing the expression

$$\chi^2(\text{age}, [\text{Z/H}]) = \sum_j \frac{(O_j - M_j)^2}{s_j^2}, \quad (1)$$

where the index $j$ runs over the selected set of spectral indices in the rest-frame range 3500–5200 Å. The main spectral indices considered in the fitting, with the exception of Fe5270, are summarized in Table 1. $O_j$ and $M_j$ are observed and model index values, respectively, where the latter depend on age and [Z/H], while the $s_j$ are the uncertainties on the observed indices. Some mild extrapolation of indices, up to [Z/H] = 0.3, has been performed following the same approach as in La Barbera et al. (2013). The resulting best-fitting light-weighted SSP equivalent age and metallicity values are $\text{age}_L = 0.24^{+0.11}_{-0.05}$ Gyr and $[\text{Z/H}]_L = 0.27^{+0.03}_{-0.20}$, respectively. The quoted errors were obtained by running the fitting procedure on a set of 100 simulated spectra (see Appendix B).

In Figure 6 the Balmer line indices measured on the spectrum of C1-23152 are compared to those expected from models at different ages and metallicity values. Hζ, Hη, Hθ, and Hι all favor high-metallicity values, consistent with D4000. $H\gamma_F$ has a very large error bar, while Hϵ and $H\delta_A$ tend to favor subsolar metallicity. The net effect is that high-metallicity values are favored from the fitting of line strengths, consistent with results from STARLIGHT (see below). Also, one should bear in mind that Hδ and Hϵ may be affected by some emission contamination, as expected from the residual star formation (in particular Hδ), reinforcing the conclusion above. The horizontal gray arrow in the Hδ panel of Figure 6 shows the value of the index corrected by 15%. This is the median correction for emission filling to Hδ absorption derived empirically by Goto et al. (2003) from a sample of 3300 local post-starburst galaxies.[12] It is reasonable to expect for Hϵ a correction not larger than the one for Hδ.

*FSF*.—In the FSF approach, stellar population models are matched to the observed spectrum in wavelength (rather than spectral index) space. To perform FSF, we have adopted the software STARLIGHT (Cid Fernandes et al. 2007; Mateus et al. 2007), which fits a linear combination of SSP models (the "base"), with different ages and metallicities, to derive the best-fitting composite model to the observed spectrum. The main advantage of this approach is that it is nonparametric, i.e., no a priori assumption on the functional form of the galaxy SFH is made. In this way, one can detect, in principle, multiple stellar components, if present, and constrain their metallicity. On the contrary, assuming a given functional form for the SFH would necessarily imply a trade-off between age, duration of star formation, and metallicity. Of course, any nonparametric approach requires the robustness of the detected stellar population components to be assessed (i.e., whether they are real, or just result from some fluctuations in the observed spectrum), as we extensively test here using Monte Carlo simulations.

STARLIGHT derives the best-fitting linear combination of SSPs using a Markov Chain Monte Carlo (MCMC) algorithm. The model spectrum is the superposition of SSPs, with age $\text{Age}_i$ and metallicity $Z_i$, each one contributing with a different fraction ($x_i$) to the light and a different fraction ($m_i$) of stellar mass, taken from a predefined set of base spectra (162 EMILES SSPs in our case). There is no restriction to the number of spectral component (SSPs) that enters in the composite model. Light-weighted ($L$) and mass-weighted ($M$) age $\text{Age}_{L,M}$ and metallicity $[\text{Z/H}]_{L,M}$ can be defined according to the relations (e.g., Asari et al. 2007)

$$\text{Age}_{L,M} = \sum_i (x_i; m_i)\text{Age}_i \quad (2)$$

and

$$[\text{Z/H}]_{L,M} = log \sum_i (x_i; m_i) Z_i / Z_\odot. \quad (3)$$

Internal reddening in the range of 0–2 mag was allowed in the fitting by considering both the Cardelli (CCM; Cardelli et al. 1989) and the Calzetti (HZ5; Calzetti et al. 2000) extinction laws, with no difference in the results. The spectral regions affected by bad sky transmission and by the presence of emission lines were masked in the fitting. The best-fitting composite model, the sum of five SSPs (see Section 5.2 for details), is shown in Figure 2 as a red curve. The corresponding mean mass-weighted stellar age (Equation (2)) is $\text{Age}_M = 400^{+30}_{-70}$ Myr (similar to that derived in Section 4.2), and metallicity (Equation (3)) is $[\text{Z/H}]_M = 0.25^{+0.006}_{-0.10}$ (second row of Table 2),[13] while the luminosity-weighted age and

[12] Other empirical methods, such as the one based on the D4000, ΔEW (Hδ) = −5.5D4000 + 11.5, provide larger corrections (30%–40%; e.g., Miller & Owen 2002).

[13] To quantify the maximum possible influence of the AGN on age and metallicity estimation, we subtracted the composite quasar spectrum by Francis et al. (1991) to the spectrum of C1-23152 and ran Starlight. The QSO spectrum was normalized to the rest-frame UV flux of the galaxy at ∼1400 Å (filters IA624, IA679) assuming that all the observed flux was due to QSO. We obtained $\text{Age}_M = 320 \pm 50$ Myr and $[\text{Z/H}] = 0.20 \pm 0.06$, respectively.

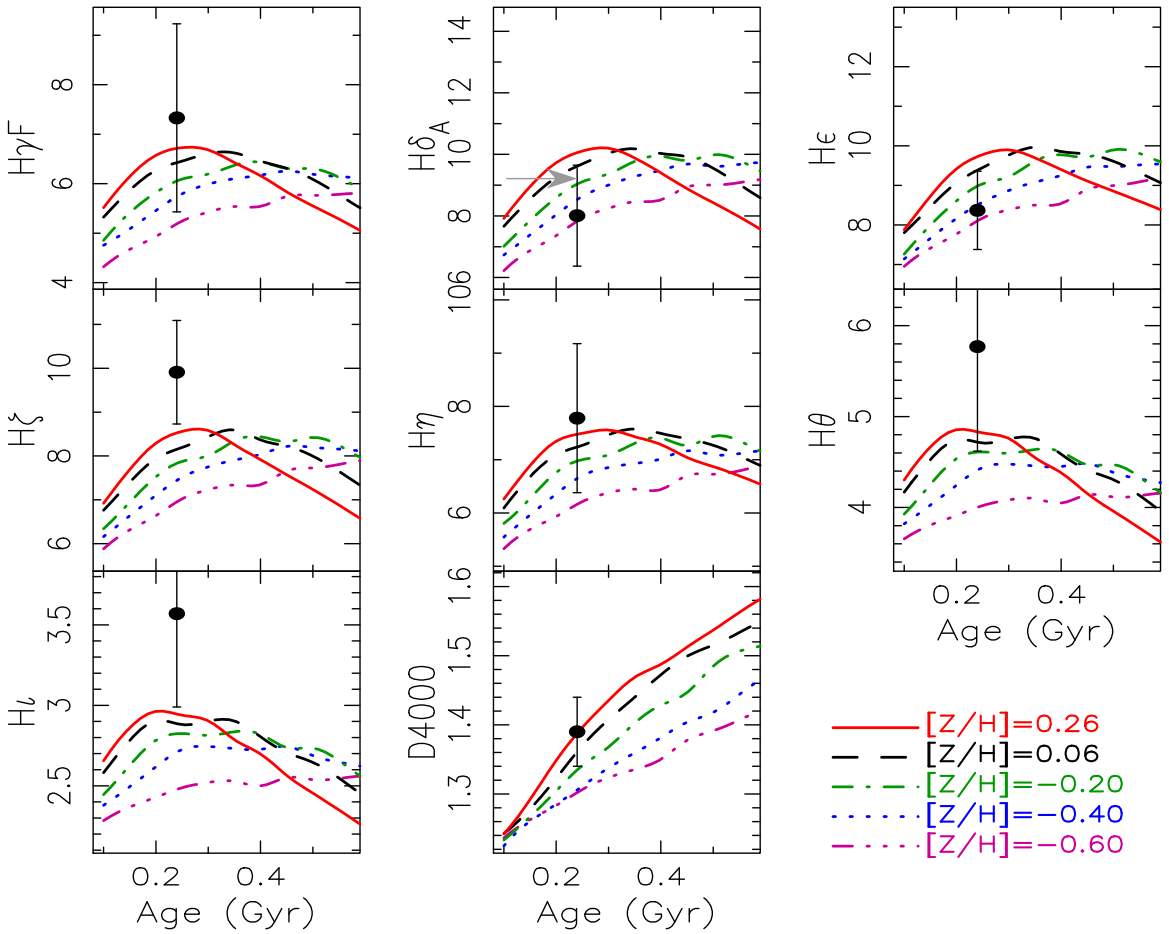


**Figure 6.** C1-23152 absorption-line strength. Balmer absorption-line indices measured on the spectrum of C1-23152 (black filled circles) are compared to those expected at different ages from EMILES SSPs with different metallicity values (colored curves). The horizontal gray arrow in the H$\delta$ panel shows the value of the index corrected by 15% to account for the average emission filling, as derived by Goto et al. (2003) for local post-starburst galaxies (see also text).

**Table 2**
Stellar Population Properties

| $Age_L$ (Gyr) | $[Z/H]_L$ | $Age_{M*}$ (Gyr) | $[Z/H]_{M*}$ | $A_V$ (mag) | IMF | Method |
|---|---|---|---|---|---|---|
| $0.24^{+0.11}_{-0.05}$ | $0.27^{+0.03}_{-0.20}$ | … | … | … | Cha | ALF |
| $0.27^{+0.05}_{-0.02}$ | $0.25^{+0.007}_{-0.11}$ | $0.40^{+0.03}_{-0.07}$ | $0.25^{+0.006}_{-0.10}$ | $0.05^{+0.06}_{-0.05}$ | Cha | FSF |
| $0.28^{+0.05}_{-0.02}$ | [0.0][a] | $0.41^{+0.03}_{-0.07}$ | [0.0][a] | $0.09^{+0.05}_{-0.05}$ | Cha | FLF[a] |
| $0.27^{+0.05}_{-0.04}$ | $0.25^{+0.00}_{-0.04}$ | $0.42^{+0.06}_{-0.09}$ | $0.25^{+0.00}_{-0.03}$ | $0.05^{+0.12}_{-0.11}$ | Sal | FSF |
| $0.23^{+0.05}_{-0.02}$ | $0.12^{+0.10}_{-0.08}$ | $0.30^{+0.05}_{-0.07}$ | $0.13^{+0.10}_{-0.08}$ | $0.19^{+0.10}_{-0.11}$ | Cha | FSF+$\alpha$-enhanced |

**Note.**
[a] This fitting has been obtained at fixed solar metallicity. Errors are assumed as those obtained with free metallicity.

metallicity are $Age_L = 270^{+50}_{-20}$ Myr and $[Z/H]_L = 0.25^{+0.007}_{-0.11}$, respectively. Notice the excellent agreement between the light-weighted age and metallicity values obtained with two independent methods, ALF and FSF. Errors (68% confidence level) and stability of best-fitting results were assessed by running STARLIGHT on a set of simulated spectra (see Appendix B).

We checked the minimum $\chi^2$ solution found by STARLIGHT by repeating the fitting with penalized PiXel-Fitting method, pPXF (Cappellari & Emsellem 2004; Cappellari 2017), which allows for regularization (see Cappellari 2017, for a comprehensive discussion of regularization in FSF). The resulting best-fitting light-weighted age and metallicity values obtained for four different degrees of regularization (parameter REGUL = 1, 2, 3, 4) are $Age_L$(Myr) = [254, 243, 213, 200] and $[M/H]_L$ = [0.20, 0.20, 0.21, 0.20], in agreement with the results obtained with other methods (see Table 2).

The degeneracy between age, metallicity, and dust has been probed by repeating the fitting with STARLIGHT at fixed metallicity for the 11 different metallicities of the EMILES library. We made use of the $F$-test to compare the $\chi^2$ of the 11 fits with the best-fitting composite model. We found that fits down to metallicity $[Z/H] = -0.60$ are still within $1\sigma$ from the best-fitting one. For this metallicity, $[Z/H] = -0.60$, the corresponding light- and mass-weighted ages are $Age_L = 420$ Myr and $Age_M = 480$ Myr with an extinction $A_V = 0.01$ mag. In Table 2, the

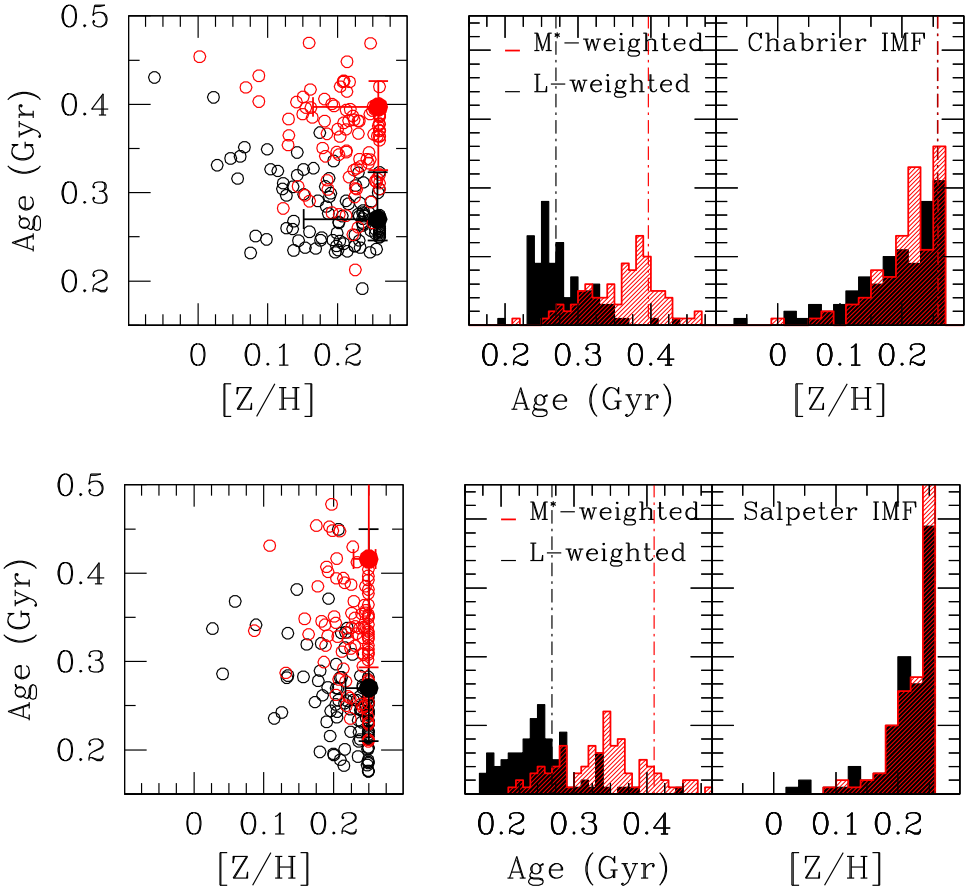


**Figure 7.** Results of FSF to simulated spectra. For each simulated spectrum, we derived age and metallicity (open circles) by running STARLIGHT as for the real spectrum. The histograms show the distributions of the estimated values. Black color identifies the light-weighted values, while red color identifies the mass-weighted values. Filled circles and dashed lines are the best-fitting values obtained for galaxy C1-23152 reported in Table 2. The top panels are the results obtained with a set of EMILES models based on a Chabrier IMF; the bottom panels are those obtained with a set of models based on a Salpeter IMF.

**Table 3**
Stellar Population Properties for Different Libraries of Models

| $\mathrm{Age}_L$ (Gyr) | $[\mathrm{Z/H}]_L$ | $\mathrm{Age}_{M*}$ (Gyr) | $[\mathrm{Z/H}]_{M*}$ | Model |
|---|---|---|---|---|
| $0.27^{+0.05}_{-0.02}$ | $0.06^{+0.10}_{-0.05}$ | $0.30^{+0.07}_{-0.05}$ | $0.10^{+0.08}_{-0.05}$ | BC03 |
| $0.80^{+0.01}_{-0.10}$ | $0.21^{+0.00}_{-0.10}$ | ... | ... | M11 |

values obtained at fixed solar metallicity are reported for reference purposes.

To test the effect of varying the IMF[14] on age and metallicity estimates, we considered also a base of SSPs with a Salpeter (Salpeter 1955) IMF. This IMF provides slightly (not significantly) older age than the Chabrier IMF, as reported in Table 2.

In the case of $\alpha$-enhanced MILES SSPs (see Section 2), the best-fitting composite model provided a mass-weighted stellar age $\mathrm{Age}_M = 300 \pm 50$ Myr and metallicity $[\mathrm{Z/H}]_M = 0.13^{+0.10}_{-0.08}$, while the luminosity-weighted values are $\mathrm{Age}_L = 230 \pm 50$ Myr and $[\mathrm{Z/H}]_M = 0.12^{+0.10}_{-0.08}$.

Finally, Table 3 lists the best-fitting age and metallicity values obtained with BC03 (Bruzual & Charlot 2003) and M11 (Maraston & Strömbäck 2011) models. The results are consistent with the reference EMILES library, with the exception of the light-weighted age obtained with M11 library, older than the others.

It is worth noting that metallicity, even if affected by larger uncertainty than age, is found to be always higher than solar ($[\mathrm{Z/H}] > 0$) independent of the models and the methods (see Tables 2 and 3). Moreover, the best-fitting metallicity values obtained for the 100 simulated spectra are all higher than solar (see Figure 7), i.e., lower-metallicity values never provide a better fit, regardless of the age and the extinction. This suggests that, actually, age, metallicity, and dust extinction are not completely degenerate with respect to absorption features and continuum shape.

Even if an acceptable fit can be obtained for subsolar metallicity values, all the results point toward a supersolar metallicity for C1-23152, regardless of the method, the models, and the IMF.

### 5.2. Stellar Populations and SFH

Figure 8 shows the contribution to the stellar mass of the different SSPs that compose the best-fitting composite model. STARLIGHT fitting detects two main stellar components (out of the five), contributing more than ~95% of the stellar mass: an older one peaked about 600 Myr prior to the epoch of observation, setting the initial formation redshift to $z_f \simeq 4.6$, and a younger one peaked 150 Myr prior to observation, constraining the redshift of quenching at $z \simeq 3.6$. The presence

[14] The effect of a time-dependent IMF and of metallicity on age and star formation timescale is discussed in Jeřábková et al. (2018) and Yan et al. (2019).

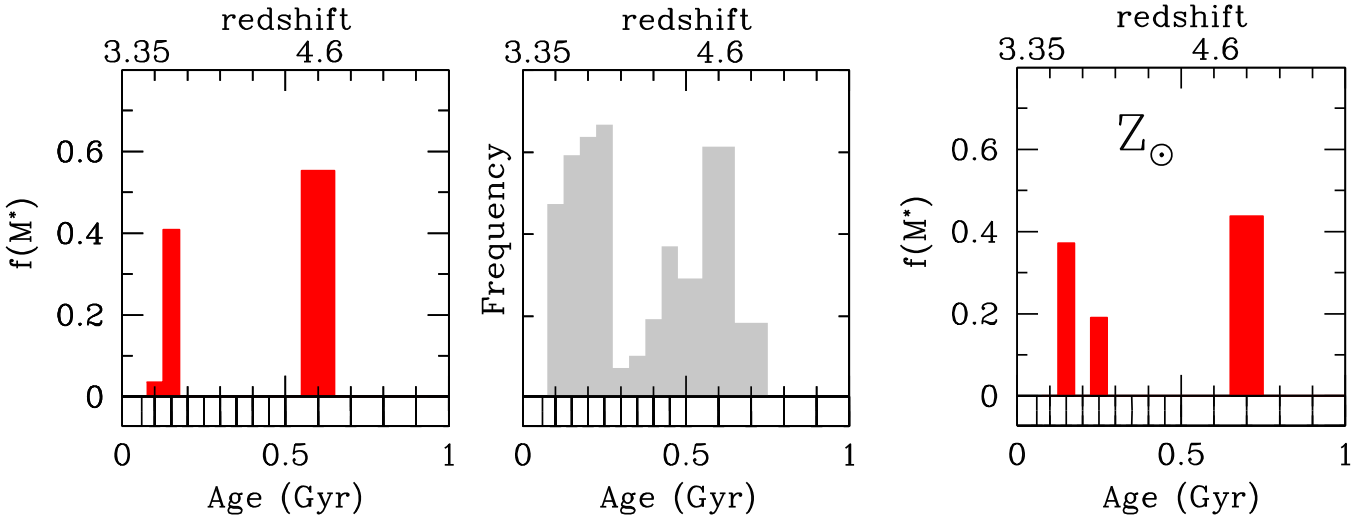


**Figure 8.** Stellar populations and SFH. The red histogram on the left panel shows the relative fraction of stellar mass associated with the SSPs that compose the best-fitting composite model of the spectrum of C1-23152 obtained with STARLIGHT (see Section 5 and second row of Table 2). The middle panel shows the distribution (gray histogram) of the best-fitting SSP components obtained by running STARLIGHT on the 100 simulated spectra (see Appendix B). The right panel is the same as the left panel but for fixed solar metallicity (see third row of Table 2). The bar code on the bottom of the figures shows the age grid of the base of SSPs.

of two main stellar components is also suggested by the distribution of the best-fitting components obtained on the 100 simulated spectra shown in the middle panel of Figure 8. The fitting at fixed metallicity described in Section 5.1 does not significantly affect the SFH in the sense that the star formation is always constrained within an interval $\Delta t_{SF} \simeq 450$–$500$ Myr with an older main component and one or more younger components. As an example, the right panel of Figure 8 shows the SFH at solar metallicity.

We probed the possible degeneracy in the solutions, by repeating the FSF with pPXF (see Section 5.1). Figure 9 shows the weighted age–metallicity map for the SSPs contributing to the best-fitting model obtained for each of the four regularization values (REGUL = 1, 2, 3, 4). In all the cases, the SFH is constrained within the interval 0.1–0.6 Gyr, with an increasing smoothness for increasing values of regularization.

These results demonstrate that the stellar population is not coeval as resulting from an SFH extended over an interval of 450–500 Myr, possibly characterized either by two main massive episodes or even by a more continuous distribution.

It is interesting to note that the spectra of quiescent galaxies at $z > 3$ reported to date appear in a post-starburst phase (see, e.g., D'Eugenio et al. 2020), as C1-23152. As such, the spectra are sensitive to the time since quenching, being dominated by the youngest stellar population (i.e., the stars formed around quenching), which outshines older stars. This effect could make it difficult to detect stellar populations formed before quenching, i.e., to infer the actual time over which galaxies formed stars and the age of the bulk of the galaxy stellar population.

We tested the ability of spectral fitting in detecting stellar populations older than the outshining youngest one, by running STARLIGHT with the same setup used for the spectrum of C1-23152, on a synthetic spectrum composed of an SSP 200 Myr old, accounting for 35% (75%) of stellar mass (flux at 4000 Å), and an SSP 1.0 Gyr old, accounting for the remaining 65% (25%).[15] The simulated spectrum and the resulting SFH are shown in Figure 10. Even if with different fractions of mass,

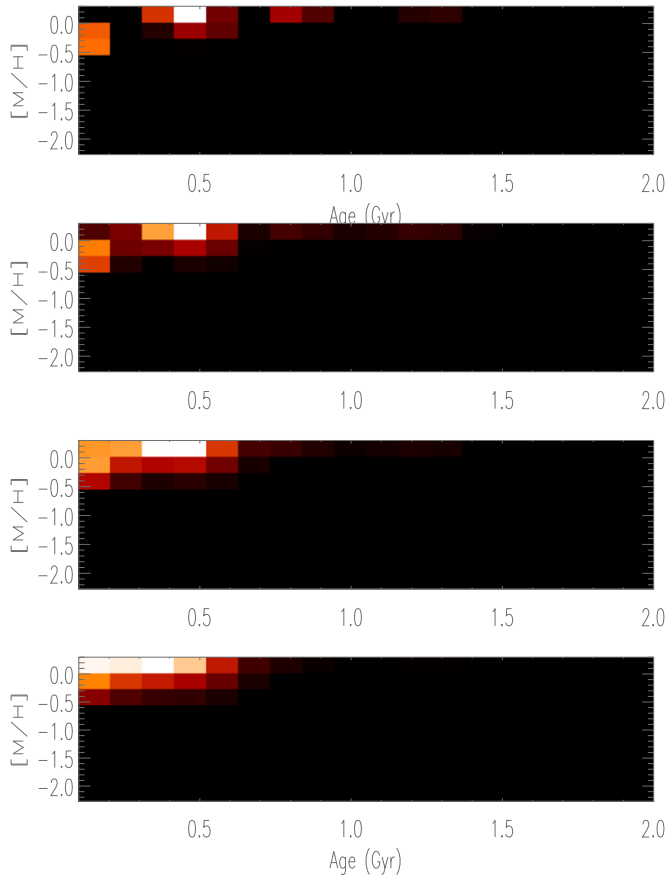


**Figure 9.** Weighted maps of the pPXF regularized solutions. Each panel shows the contribution of the SSPs composing the best-fitting composite model in the different age and metallicity intervals considered. The four maps have been obtained for four different values of regularization (from top to bottom), REGUL = [1, 2, 3, 4]. The corresponding light-weighted age and metallicity values are $\mathrm{Age}_L$(Myr) = [254, 243, 213, 200] and $[\mathrm{M/H}]_L$ = [0.20, 0.20, 0.21, 0.20], in agreement with the results obtained with the other methods (see Table 2). The SSPs contributing to the best-fitting model are all in the age range 0.1–0.6 Gyr, confirming the interval of the star formation derived with STARLIGHT and roughly constrained in Section 4.2.

[15] See Cid Fernandes et al. (2005) for the robustness of STARLIGHT in recovering different SFHs.

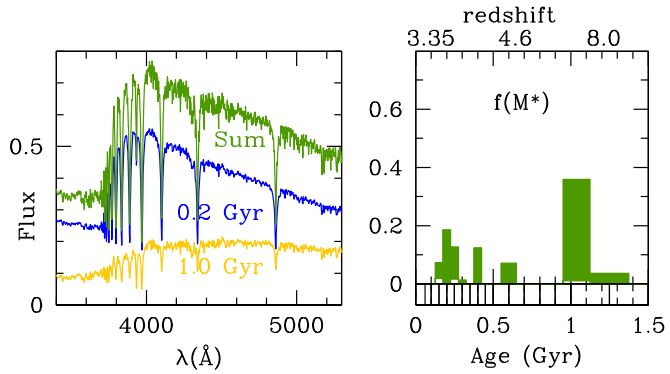


**Figure 10.** Left: simulated spectrum (green curve) sum of an SSP 0.2 Gyr old (blue curve), representing 35% of the stellar mass (75% of the flux at 4000 Å), and an SSP 1.0 Gyr old (yellow curve), accounting for the remaining 65% (25%). Right: relative fraction of stellar mass associated with the SSPs that compose the best-fitting composite model to the simulated spectrum. The bar code on the bottom shows the age grid of the base of SSPs.

the two components have been detected, constraining the time since quenching (youngest) and the time since the first important episode of star formation (oldest). Therefore, we are confident that the SFH found for C1-23152 is not affected by the major contribution in light from the youngest population.

The analysis shows that the buildup of C1-23152 has taken place in about $\Delta t_{\rm build} \simeq 600$ Myr as constrained by the oldest stellar component, i.e., in the range $3.35 < z < 4.6$. The youngest stellar component constrains the time since quenching at $t_{\rm quench} \sim 150$ Myr, in agreement with the upper limit to the current SFR ($<6.5\ M_\odot\ {\rm yr}^{-1}$) and with the constraints derived in Section 4.2. It follows that the stellar mass ($\sim 2 \times 10^{11}\ M_\odot$; see below) has been formed in an interval $\Delta t_{\rm SF} \simeq 450$–$500$ Myr, corresponding to an average $\overline{\rm SFR} > 400\ M_\odot\ {\rm yr}^{-1}$. If the SFH was characterized by the two main episodes of star formation (Figure 8), their SFR would be $\sim 1200\ M_\odot\ {\rm yr}^{-1}$.[16]

We also adopted an independent approach by using FAST++ (Kriek et al. 2018; Schreiber et al. 2018)[17] to perform a simultaneous parametric fitting of the spectrum and the multi-wavelength UltraVISTA photometry. The fitting is described in detail in Appendix A. According to the adopted SFHs (a delayed exponentially declining SFH and a double exponentially increasing/decreasing SFH), the buildup of the galaxy would be realized in less than 250 Myr prior to observations (mass assembly $3.35 < z < 3.8$), a time significantly shorter than the one obtained through FSF. The resulting mean stellar age is younger than the ages obtained through ALF and STARLIGHT. This approach deals principally with broad/narrowband photometry, i.e., with the stars producing the dominant light. Therefore, in this case, the youngest stellar population could affect the results (see, e.g., Maraston et al. 2010; Greggio & Renzini 2011).

### 5.3. Stellar Mass Estimate

To estimate the stellar mass of C1-23152, we adopted different approaches: (i) We relied on the STARLIGHT FSF results, using the relation $M^* = m_{\rm ini} \times 4\pi d^2_L / M_\odot$ (Cid Fernandes et al. 2007), where $m_{\rm ini}$ is the normalization factor of the EMILES composite model to obtain the observed flux and $d_L$ is the luminosity distance. This approach provides $M^* = 1.5\ (\pm 0.2) \times 10^{11}\ M_\odot$ after having normalized the spectrum to the observed $K$-band flux ($K_{AB} = 20.31$) of C1-23152. (ii) We used the result of ALF (see above). We normalized the EMILES SSP model corresponding to ${\rm age}_L = 0.24$ Gyr and $Z_L = 0.27$ to match the $V$-band rest-frame flux of C1-23152 from Marsan et al. (2015). This provides a stellar mass estimate of $M^* = 1.0 \times 10^{11}\ M_\odot$. (iii) We used the outputs of FAST++ (see Appendix A) based on BC03 models, which provide values in the range $M^* = (2.6$–$3.1^{+0.5}_{-0.0}) \times 10^{11}\ M_\odot$ (consistent with the estimate by Marsan et al. 2015, $M^* = 2.8^{+0.6}_{-0.7} \times 10^{11}$, based on SED fitting, scaled to Chabrier IMF). Combining all these values, we obtain a final estimate of $M^* = 2.0\ (\pm 0.7) \times 10^{11}\ M_\odot$,[18] consistent with the constraint imposed by the dynamical mass (see below). The uncertainty accounts for the different estimates of $M^*$, based on different methods, software, and models. The resulting stellar mass density within $R_e$ is $\Sigma_e^{M^*} = \Sigma_{\rm 1kpc} = 3.2\ (\pm 0.7) \times 10^{10}\ M_\odot\ {\rm kpc}^{-2}$, where $\Sigma_e^{M^*} = 0.5 M^*/(\pi R_e^2)$, i.e., we assumed that the stellar mass profile follows the luminosity profile of the galaxy.

### 5.4. Stellar Velocity Dispersion Measurement and Dynamical Mass Estimate

A velocity dispersion measurement was performed by fitting the observed spectrum using pPXF (Cappellari & Emsellem 2004; Cappellari 2017). The fitting was performed by masking out the regions with emission lines ([OII], H$\beta$, [OIII]) and the region of low atmospheric transmission (18000–19000 Å) between $H$ and $K$ bands (see Figure 2). In the fitting, a Legendre polynomial with degree = 4 is added to correct the template continuum shape during the fit. We verified that the result does not depend on the polynomial degree by varying it in the range 1–4. The stability of the measurement with respect to the wavelength range considered was tested by shifting and varying the width of the masked regions by about 200 Å and by fitting the H-band data only. In all the cases considered, we obtained values within 5% of our nominal $\sigma$ estimate. The dependence of the velocity dispersion measurements on the library of templates used was tested by repeating the fitting to the observed spectrum with different libraries of SSP models, EMILES-Padova (Vazdekis et al. 2015), BC03, and M11. These additional sets of templates provided values within 6% from the reference value.[19]

The galaxy stellar velocity dispersion $\sigma_*$ was derived from the relation $\sigma_*^2 = \sigma_{\rm obs}^2 - \sigma_{\rm inst}^2 - \sigma_{\rm stack}^2$, where $\sigma_{\rm obs} = 396\ {\rm km\ s}^{-1}$ is the velocity dispersion resulting from the pPXF spectral fitting, $\sigma_{\rm inst} \sim 100\ {\rm km\ s}^{-1}$ is the broadening due to the instrumental resolution, and $\sigma_{\rm stack} \sim 10\ {\rm km\ s}^{-1}$ is the broadening due to the uncertainty in the wavelength calibration of the frames. The robustness of the $\sigma_{\rm obs}$ estimate was tested by repeating the

[16] We used Equation (5) in Asari et al. (2007), and we derived the SFR as the ratio of the fraction of mass in the burst to the age bin size, considering that the age resolution of the models is 100 Myr for age >500 Myr and 50 Myr at younger ages. Therefore, this SFR is a lower limit driven by the age resolution of the models.

[17] https://github.com/cschreib/fastpp

[18] For a Salpeter IMF, given the ages as measured in Table 2, the stellar mass is a factor of ~1.3 larger than for a Chabrier IMF (as derived from EMILES models), i.e., $M^* = 2.6\ (\pm 0.7) \times 10^{11}\ M_\odot$.

[19] Velocity dispersion measurement based primarily on Balmer lines, dominated by high rotational velocity A-type stars, may be subject to systematics if the correct stellar population is not matched (e.g., Belli et al. 2017). We tested for possible systematics by repeating the fit with stellar spectra from the Indo-US library (Valdes et al. 2004), first using only F, G, and K stars, then including also A stars. We obtained, in the two cases, $\sigma_{\rm obs} = 410 \pm 41\ {\rm km\ s}^{-1}$ and $\sigma_{\rm obs} = 384 \pm 48\ {\rm km\ s}^{-1}$ respectively, with the value obtained using stellar population synthesis models ($\sigma_{\rm obs} = 396\ {\rm km\ s}^{-1}$) in between.

**Table 4**
Physical Properties of C1-23152

| Parameter | Value | Comment |
|---|---|---|
| Redshift, $z$ | $3.352 \pm 0.002$ | From Marsan et al. (2015) |
| Effective radius, $R_e$ | $1.0 \pm 0.1$ kpc | In F160 band from Marsan et al. (2015) |
| Sérsic index, $n$ | 4.4 | In F160 band from Marsan et al. (2015) |
| Stellar velocity dispersion, $\sigma_e$ | $409 \pm 60$ km s$^{-1}$ | Scaled to the effective radius |
| Age$_{M^*}$ | $400^{+30}_{-70}$ Myr | Age of the bulk of stellar mass |
| Metallicity [Z/H] | $0.25^{+0.006}_{-0.10}$ | Expressed as log(Z/Z$_\odot$) |
| Extinction, A$_V$ | $0.05^{+0.06}_{-0.05}$ mag | |
| Dynamical mass, $M_{\rm dyn}$ | $2.2(\pm 0.4) \times 10^{11}\ M_\odot$ | From Equation (4) |
| Stellar mass, $M^*$ | $2.0(\pm 0.7) \times 10^{11}\ M_\odot$ | Mean of different estimates |
| Current SFR | $< 6.5\ M_\odot$ yr$^{-1}$ | H$\beta$ emission-line limit |
| Buildup timescale, $\Delta t_{\rm build}$ | $600 \pm 100$ Myr | $3.35 < z < 4.6$ assembly of galaxy |
| Time since quenching, $t_{\rm quench}$ | $150 \pm 50$ Myr | Time since last burst |
| Stellar mass formation, $\Delta t_{\rm SF}$ | $450 \pm 110$ Myr | Interval of star formation |
| Average SFR within $\Delta t_{\rm SF}$ | $440 \pm 110\ M_\odot$ yr$^{-1}$ | SFR required to form $M^*$ in $\Delta t_{\rm SF}$ |

measurement for a set of 100 simulated spectra (see Appendix B). We estimated $\sigma_* = 383 \pm 60\,{\rm km\,s^{-1}}$ within a diameter aperture of $2r = 0\farcs75$ (the slit width). The resulting velocity dispersion within the effective radius $R_e = 1$ kpc (Marsan et al. 2015) is $\sigma_e = 409 \pm 60$ km s$^{-1}$, where we used the relation $\sigma_*/\sigma_e = (r/r_e)^{-0.065}$ (Jørgensen et al. 1995; Cappellari et al. 2006)[20].

The dynamical mass $M_{\rm dyn}$ of the galaxy has been derived from the velocity dispersion $\sigma_e$ and the effective radius $R_e$ through the relation

$$M_{\rm dyn} = k_n \frac{\sigma_e^2 R_e}{G}, \quad (4)$$

where $G$ is the gravitational constant and $k_n$ is the virial coefficient that takes into account the distribution of both luminous and dark matter (DM) and the projection effects (Bertin et al. 2002; Lanzoni & Ciotti 2003). We used $k_n = 8.88 - 0.831n + 0.0241n^2$ (Cappellari et al. 2006)[21] with Sérsic index $n = 4.4$, as resulting from surface brightness fitting (Marsan et al. 2015). We thus obtained $M_{\rm dyn} = 2.2 \pm 0.4 \times 10^{11}\ M_\odot$.

We note that, in the case of a Chabrier IMF, the DM fraction is less than 10%, even if with large errors ($f_{\rm DM}(Cha) = (M_{\rm dyn} - M^*)/M_{\rm dyn} = 0.09 \pm 0.3$), while for a Salpeter IMF $f_{DM}(Sal) = -0.18 \pm 0.3$, still consistent with a null fraction. These results suggest that the DM fraction within the effective radius is extremely low in massive dense ETGs, as already noticed in ETGs at $z \sim 1.3$ (Saracco et al. 2020), and that a bottom-heavy IMF (higher ratio of low- to high-mass stars) is disfavored in dense ETGs, irrespective of their redshift (Gargiulo et al. 2015). Notice that, based on results at $z \sim 0$, a bottom-heavy IMF is expected to be confined in the very central regions of galaxies, making the integrated stellar mass-to-light ratio within the effective radius below the expectation for a Salpeter IMF (see, e.g., La Barbera et al. 2019). However, our observations virtually collect the whole object light and cannot detect this effect.

[20] This correction is derived from observations of local resolved galaxies. However, being a power law, it can be applied also to spatially unresolved galaxies, as is the case for C1-23152.

[21] We note that the relations relevant to dynamical properties of galaxies heavily rely on local studies. It is uncertain whether these relations can be applied as they are also to galaxies in the early universe. However, we noticed that, for a theoretical value of $K_n = 5$, the dynamical mass and the DM fraction would change by about 13%.

## 6. Discussion and Conclusions

### 6.1. The Formation of a Massive ETG at High z

The analysis of the LBT-LUCI spectrum of the galaxy C1-23152 has lead to the following results (summarized in Table 4). C1-23152 is an ETG hosting an AGN at $z = 3.35$ that assembled $2.0\ (\pm 0.5) \times 10^{11}\ M_\odot$ of stars, quenched its star formation, and shaped its morphology in the ~600 Myr preceding the observation, i.e., between $3.35 < z < 4.6$, as constrained by the oldest stellar component detected in the galaxy. This fast buildup is significantly shorter than that expected based on dynamical friction merging timescales, larger than 2–3 Gyr (e.g., Boylan-Kolchin et al. 2008). The short assembly time suggests that the stellar mass growth has taken place in situ through highly dissipative processes rather than ex situ through mergers of preexisting stellar systems (e.g., Kroupa et al. 2020).

The high stellar velocity dispersion, $\sigma_e = 409 \pm 60$ km s$^{-1}$, confirms the high mass, $M_{\rm dyn} = 2.2\ (\pm 0.4) \times 10^{11}\ M_\odot$, and the high mass density of the galaxy. The surface stellar mass density within $R_e$ is $\Sigma_e^{M^*} = \Sigma_{1\rm kpc} = 3.2\ (\pm 0.7) \times 10^{10}\ M_\odot$ kpc$^{-2}$ ($\Sigma_e^{M_{\rm dyn}} = 3.5\ (\pm 0.5) \times 10^{10}\ M_\odot$ kpc$^{-2}$), comparable to the density of the densest and most massive ETGs in the local universe, as shown in Figure 11. This high mass density coherently argues for a highly dissipative formation process as expected theoretically (e.g., Hopkins et al. 2010; Lapi et al. 2018) and from the empirical Kennicutt-Schmidt law (Kennicutt 1998a). This fast dissipative process could result from a cosmological merger of gas-dominated systems (e.g., Naab et al. 2007) or from violent instability of a gas-rich disk (Dekel & Burkert 2014) and points toward a role of the density in regulating the quenching process (Woo et al. 2015; Tacchella et al. 2016).

The whole stellar mass observed at $z = 3.35$ has been formed within a short interval, $\Delta t_{\rm SF} \simeq 450$ Myr, corresponding to an average $\overline{\rm SFR} > 400\ M_\odot$ yr$^{-1}$, possibly through two main episodes of star formation or through a continuous episode. The resulting stellar population has a mean mass-weighted Age$_M = 400^{+30}_{-70}$ Myr. The supersolar metallicity [Z/H] = $0.25^{+0.006}_{-0.10}$ agrees with a fast dissipative process and points toward a star formation efficiency much higher than the

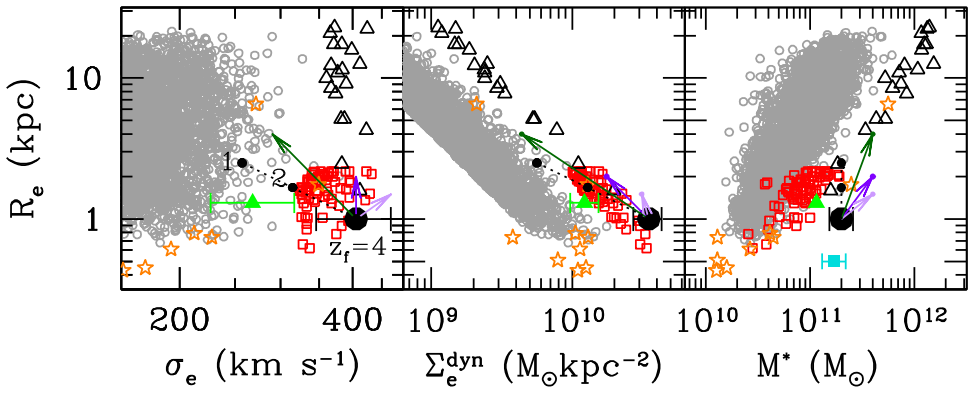


**Figure 11.** Physical properties of C1-23152 and of ETGs in the local universe. The half-light radius $R_e$ of galaxy C1-23152 (black filled circle) is plotted against (from left to right) velocity dispersion $\sigma_e$, surface mass density $\Sigma_e^{\rm dyn}$, and stellar mass $M^*$ and compared to the same parameters of other ETGs in the local universe (open symbols) and at redshift $z > 3$ (filled symbols). For the local universe, the gray circles represent ETGs selected from SPIDER sample (La Barbera et al. 2010), the black triangles are ETGs with $\sigma_e > 350$ km s$^{-1}$ (Bernardi et al. 2006), the red squares are compact ETGs with high velocity dispersion (Saulder et al. 2015), and the orange stars are compact ETGs missed by the SDSS (Damjanov et al. 2015). At redshift $z > 3$, the properties of C1-23152 are compared with those of a galaxy at $z \simeq 4$ (Tanaka et al. 2019, 2020) (green filled triangle) and an ETG at $z \simeq 3.7$ (Glazebrook et al. 2017) (light-blue square). The arrows indicate the paths for C1-23152 to grow in stellar mass by a factor of 2 from $z = 3.35$ to $z = 0$ by experiencing a wet merger (light-purple arrow), during which a significant fraction of the additional stellar mass is formed through dissipative processes; a major equal-mass ∼(1:1) dry merger (purple arrow); and accretion of small systems (dark green) with mass ratio ∼(1:10) (see text). The small black circles connected by a dashed line represent the properties that a C1-23152-like galaxy would have if it forms at redshift $1 < z_f < 4$, assuming that its properties (equal to those of C1-23152 at $z = 4$) scale according to the matter density of the universe, where we assumed $\rho_m(z) \propto (1+z)^3$.

replenishment time of the gas, resembling a nearly closed-box enrichment. Supersolar metallicity ($[Z/H] = 0.13^{+0.10}_{-0.08}$) is also obtained when $\alpha$-enhanced models are considered. These abundance ratios may better match the overabundance of [Mg/Fe] observed in local massive ETGs (e.g., Worthey et al. 1992), overabundance usually interpreted as a result of short formation timescales (<1 Gyr; see, e.g., Trager et al. 2000; Renzini 2006). Indeed, Vazdekis et al. (1996) show that, in the case of a closed-box regime, supersolar metallicity can be reached just within the first 100–200 Myr of star formation, a timescale comparable to the star formation of C1-23152 (see also Pantoni et al. 2019). It is interesting to note that, in this approximation, the expected final extinction is negligible, as indicated by the virtually null value ($A_V = 0.05 \pm 0.05$) obtained by spectral fitting.

The star formation in C1-23152 has halted ∼100–150 Myr before observation, leaving a residual star formation <6.5 $M_\odot$ yr$^{-1}$. Therefore, the quenching mechanism must have been extremely efficient to reduce the star formation to a few $M_\odot$ yr$^{-1}$ in less than 150 Myr. The presence of an AGN could explain the fast quenching even if it is usually associated with a powerful outflow (e.g., Cicone et al. 2014; Maiolino et al. 2012) whose presence is difficult to assess from our data. Our analysis cannot establish a causality between the high mass density or the AGN and the extremely fast suppression of star formation. On the other hand, this study suggests that they can play a role in the very fast quenching process of massive galaxies in the early universe.

### 6.2. The Evolution of a Massive ETG since z = 3.35

Figure 11 compares the physical properties (effective radius, velocity dispersion, surface mass density, and stellar mass) of C1-23152 (big black points) with those of local ETGs with comparable mass (see Section 2). In particular, for the local universe, we considered ETGs selected from SPIDER sample (gray circles; La Barbera et al. 2010), the ETGs with $\sigma_e > 350$ km s$^{-1}$ from Bernardi et al. (2006) (black triangles), the compact ETGs with high velocity dispersion selected by Saulder et al. (2015) (red square), and the compact ETGs missed by the SDSS and identified by Damjanov et al. (2015) (orange stars). At redshift $z > 3$, the properties of C1-23152 are compared with those of the galaxy at $z \simeq 4$ (Tanaka et al. 2019, 2020) (green filled triangle) and an ETG at $z \simeq 3.7$ (Glazebrook et al. 2017) (light-blue square).

The evolutionary path that C1-23152 will follow in the subsequent ∼12 Gyr, whether minor merger will increase its size, and/or a secondary burst of star formation will rejuvenate the mean stellar age, or a major merger will increase its mass and size, or it will arrive unperturbed to $z = 0$, cannot be univocally determined. However, we investigated the properties of the possible descendant of C1-23152 according to the different evolutionary paths that the galaxy could follow.

In an equal-mass (1:1) dry merger, the growth in stellar mass is approximately the same as the growth in size (e.g., Ciotti et al. 2007; Hopkins et al. 2009). Consequently, the velocity dispersion remains nearly constant, and the surface mass density decreases as the size increases. This case is shown in Figure 11 by the purple arrow for a mass increase by a factor of 2, i.e., for a single major merger as expected for high-mass galaxies (e.g., De Lucia et al. 2006).

If a mass increase by a factor of 2 occurs via a major wet merger during which a significant fraction of the additional stellar mass is formed in situ through star formation, then the size of the resulting galaxy increases less than a factor of 2, depending on the fraction of mass involved in the dissipative process (Ciotti et al. 2007; Hopkins et al. 2009). Consequently, the velocity dispersion slightly increases, as the square root of the ratio between the mass and the size of the final system, while the surface density scales as the ratio between mass and the square of the radius. This case is shown by the light-purple arrow in Figure 11, representing a size increase by a factor of 1.5.

Finally, if the mass increase is due to accretion of very small systems, i.e., minor mergers, then the size increase is greater than that observed for the dry major merger scenario. For a mass increase by a factor of 2 and assuming a single merger of mass ratio ∼(1:10), the radius grows by a factor of 4, while the

velocity dispersion and the stellar mass surface density decrease by a factor of ∼1.4 and 8, respectively (Ciotti et al. 2007; Hopkins et al. 2009; Naab et al. 2009; Bezanson et al. 2009). This case is shown by the dark-green arrow in Figure 11.

The cases considered show that C1-23152 will hardly grow its mass significantly through dissipative processes since the resulting galaxy would have a mass density and velocity dispersion higher than those of the densest and highest velocity dispersion ETGs in the local universe. On the other hand, a mass growth through dry major or minor merging is instead conceivable (but see Nipoti et al. 2009, for the large scatter introduced by dry mergers in the scaling relations).

It is worth noting that Marchesini et al. (2014), using a semiempirical approach based on abundance matching, find that the likely progenitors of local ultramassive galaxies (log $(M^*) \simeq 11.8\ M_\odot$) grow by $0.56^{+0.35}_{-0.25}$ dex in stellar mass since $z = 3$, i.e., their mass at $z \sim 3$ is (2–3) $\times\ 10^{11}\ M_\odot$, consistent with the mass of C1-23152 (see also Kubo et al. 2018, for a discussion on the size evolution of galaxies since $z \sim 4$).

Finally, Figure 11 shows also that the densest massive ETGs in the local universe share the same extreme physical properties of C1-23152 at $z = 3.352$. Theoretically, it is established that, at all redshifts, dissipation is the most important factor determining the mass density and, hence, size of galaxies (e.g., Hopkins et al. 2009). Given the higher density of the universe and the larger gas fractions at high redshift, densest galaxies are expected to form in the early universe (Hopkins et al. 2010). Accordingly, lower-redshift formation implies less dense galaxies. In Figure 11, the dashed line connecting small black circles represents the properties that a C1-23152-like galaxy would have, if it forms at redshift $1 < z_f < 4$, assuming that its properties (equal to those of C1-23152 at $z_f = 4$, for simplicity) scale as the matter density of the universe, where we assumed the simple scaling relation $\rho_m(z) \propto (1 + z)^3$.

If the densest galaxies form at high redshift, they should host the oldest stellar populations. Indeed, observations have established that, at fixed mass, denser galaxies host older stars irrespective of their redshift (e.g., Saracco et al. 2009, 2011; Valentinuzzi et al. 2010), and consequently, their formation epoch precedes the one of less dense galaxies (e.g., Estrada-Carpenter et al. 2020; Saracco et al. 2020). Therefore, even if C1-23152 may follow different possible evolutionary paths, the densest massive ETGs in the local universe most likely have a C1-23152-like galaxy as a progenitor that arrived unperturbed to $z = 0$, since their extreme properties require physical conditions for their formation similar to those for C1-23152, difficult to realize at lower redshift.

This work is based on observations carried out at the Large Binocular Telescope (LBT) under the observation program 2017B-C2743-3 (P.I. Paolo Saracco). The LBT is an international collaboration among institutions in Italy, Germany, and the United States. LBT Corporation partners are Istituto Nazionale di Astrofisica (INAF), Italy; LBT Beteiligungsgesellschaft, Germany, representing the Max-Planck Society, the Leibniz Institute for Astrophysics Potsdam, and Heidelberg University; the University of Arizona on behalf of the Arizona Board of Regents; The Ohio State University; and the Research Corporation, on behalf of the University of Notre Dame, University of Minnesota, and University of Virginia. We acknowledge the support from the LBT-Italian Coordination Facility for the execution of the observations, the data distribution, and support in data reduction. P.S. would like to thank R. Paulson and the Mayhem project. D.M. and M.A. acknowledge support by grant No. NNX16AN49G issued through the NASA Astrophysics Data Analysis Program (ADAP). Further support was provided by the Faculty Research Fund (FRF) of Tufts University. F.L.B. acknowledges support from grant AYA2016-77237-C3-1-P from the Spanish Ministry of Economy and Competitiveness (MINECO). G.W. acknowledges support by the National Science Foundation through grant AST-1517863, by HST program No. GO-15924, and by grant No. 80NSSC17K0019 issued through the NASA Astrophysics Data Analysis Program (ADAP). Support for program No. GO-15294 was provided by NASA through a grant from the Space Telescope Science Institute, which is operated by the Association of Universities for Research in Astronomy, Incorporated, under NASA contract NAS5-26555.

## Appendix A
## FAST++ Fitting

A great advantage of FAST++ is that the whole SED can be considered in the fitting, simultaneously modeling the photometry and the spectrum. However, the best-fitting model is chosen among a set of model templates whose SFH is defined a priori. Any SFH implies a trade-off between stellar age and duration of the star formation to best match the data. Therefore, the resulting age, the interval within which the star formation can have taken place, and the SFR depend on the adopted SFHs. Metallicity is not a free parameter in the fitting, as it is fixed with the choice of adopted models. We considered BC03 models with a Chabrier (2003) IMF and Calzetti et al. (2000) extinction law. Two SFHs were considered: a delayed exponentially declining SFH ($\tau$-mod hereafter) with $e$-folding time $\log(\tau/\mathrm{yr}) = [7\text{–}10]$ with step 0.1 and $\log(\mathrm{age}/\mathrm{yr}) = [7\text{–}9]$ with step 0.05, and a double exponential ($2\tau$-mod hereafter; e.g., Schreiber et al. 2018) exponentially increasing ($\log(\mathrm{trise}/\mathrm{yr}) = [7\text{–}9.5]$ with step 0.5) and exponentially decreasing ($\log(\mathrm{tdecl}/\mathrm{yr}) = [7\text{–}9.5]$ with step 0.5). In both cases, a recent burst was allowed to be present. For each of these two SFHs, a solar metallicity ($Z = 0.02$) and supersolar metallicity ($Z = 0.05$) were adopted. For C1-23152, we fit together the LBT spectrum and the multiwavelength UltraVISTA photometry composed of 49 bands. In addition to the 30 photometric bands used in the construction of the UltraVISTA DR1 catalog of Muzzin et al. (2013), photometry from the following images was included: ultradeep optical imaging from HSC (Tanaka et al. 2017), the UltraVISTA DR3 *YJHK* (∼1.2 mag deeper than the DR1 images), deeper (by ∼1 mag) IRAC photometry from SPLASH (Mehta et al. 2018) and SMUVS (Caputi et al. 2017; Ashby et al. 2018), UltraVISTA NB118, five CFHTLS deep optical images, and medium-band near-IR images from the NMBS (see A. Muzzin et al. 2020, in preparation).

In all the cases, the SED+spectrum excluded the presence of a recent burst. For $Z = Z_\odot$ ($2.5\ Z_\odot$), in the $\tau$-mod case, the star formation starts 251 (224) Myr prior to observation and 50% of the mass (2.9 (2.6) $\times\ 10^{11}\ M_\odot$) is formed in about 42 (42) Myr at a mean SFR $\sim$ 3430 (3060) $M_\odot\ \mathrm{yr}^{-1}$. The star formation drops to 10% 123 (96) Myr prior to observation, leaving a residual SFR = 8 (19) $M_\odot\ \mathrm{yr}^{-1}$. The extinction is $A_V = 0.5$ (0.4) mag.

The $2\tau$-mod SFH implies a slightly faster buildup and quenching (and larger peak of star formation): for $Z = Z_{\odot}$ ($2.5\ Z_{\odot}$), the star formation starts 224 (178) Myr prior to observation and 50% of the mass ($3.1\ (2.7) \times 10^{11}\ M_{\odot}$) is formed in 38 (8) Myr at a mean SFR $\sim 4066\ (16800)\ M_{\odot}\ \mathrm{yr}^{-1}$. The star formation drops to 10% 135 (151) Myr prior to observation, leaving a residual SFR $= 25\ (23)\ M_{\odot}\ \mathrm{yr}^{-1}$. The extinction is $A_V = 0.6\ (0.4)$ mag.

Therefore, according to the adopted SFHs, the buildup of C1-23152 would be realized in less than 250 Myr, i.e., between $3.35 < z < 3.8$. The resulting mean stellar age is younger than the ages obtained with STARLIGHT for the same BC03 models (see Table 3) and with the ALF method, and the buildup of the galaxy is significantly shorter.

## Appendix B
## Simulations

The robustness of age, metallicity, and velocity dispersion measurements was assessed by repeating the fitting to two sets of 100 simulated spectra having the same S/N of the observed spectrum. The first set (MC-set hereafter) was obtained through a Monte Carlo approach, i.e., by varying the value of the true observed spectrum $f_{\mathrm{obs}}(\lambda)$ by a shift $\delta f$ randomly chosen from a Gaussian distribution with sigma $df(\lambda)$, the error on $f_{\mathrm{obs}}(\lambda)$. The second set of simulated spectra (R-set hereafter) was obtained by summing to the best-fitting model template $f_{\mathrm{mod}}(\lambda)$ the residuals $R(\lambda) = f_{\mathrm{obs}}(\lambda) - f_{\mathrm{mod}}(\lambda)$ randomly shuffled in wavelength within windows 200 Å wide, along the wavelength axis, i.e., $f_{\mathrm{sim}}(\lambda) = f_{\mathrm{mod}}(\lambda) + R(\lambda_{\mathrm{RND}})$.

The distributions of the best-fitting values obtained with the two sets of simulated spectra do not differ significantly. However, R-set has the advantage to take into account possible systematics in the observed spectrum due to sky residuals or sky absorptions. Reshuffling allows for considering the effects of these systematics both in the absorption-line fitting and in the FSF. For these reasons, we consider the results obtained from R-set as a reference.

The results of the absorption-line fitting obtained with R-set of simulated spectra is shown in Figure 12, while Figure 7 shows the results obtained with FSF (STARLIGHT). To quantify the dependence of the results on the IMF assumed, for each simulated spectrum we measured age and metallicity by running STARLIGHT using the same parameter setup and two bases of SSP models, one based on a Chabrier IMF and the other on a Salpeter IMF, as for the observed spectrum of galaxy C1-23152. The distribution of the best-fitting extinction values $A_V$ is always constrained within low values, with a median extinction $A_V = 0.06 \pm 0.06$ mag in the case of a Chabrier IMF and $A_V = 0.08 \pm 0.09$ mag in the case of a Salpeter IMF. Figure 7 shows the results obtained for the two different IMFs. The Salpeter IMF provides best-fitting mass-weighted ages with a slightly larger spread with respect to the Chabrier IMF. Notice that the differences due to varying the IMF are not significant. The errors at 68% confidence level reported in Table 1 for galaxy C1-23152 are derived from the distribution of the best-fitting values obtained from these simulations.

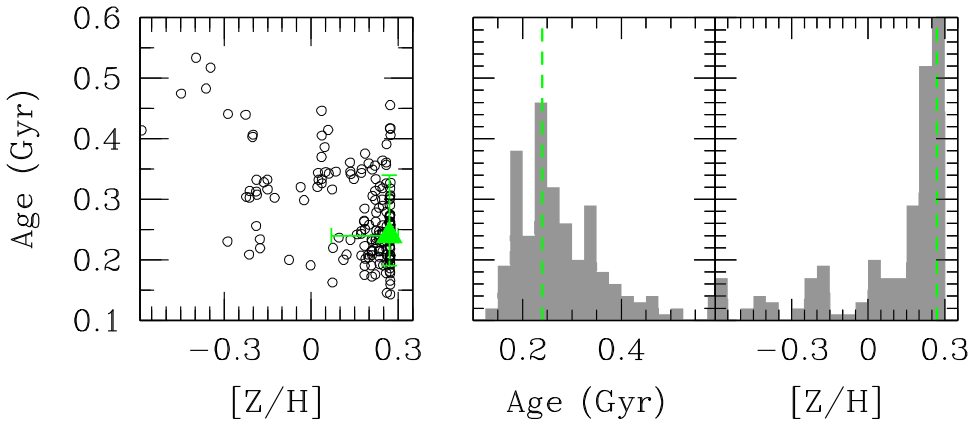


**Figure 12.** Results of absorption-line fitting to the 100 simulated spectra. For each simulated spectrum (see Section B), the best-fitting age and metallicity have been found by comparing the measured line strengths to those predicted by SSP with varying age and metallicity. The histograms show the distributions of the best-fitting values. The green filled triangle and dashed lines mark the best-fitting values obtained for C1-23152 reported in Table 2.

## ORCID iDs

Paolo Saracco https://orcid.org/0000-0003-3959-2595
Danilo Marchesini https://orcid.org/0000-0001-9002-3502
Ben Forrest https://orcid.org/0000-0001-6003-0541
Z. Cemile Marsan https://orcid.org/0000-0002-7248-1566
Adam Muzzin https://orcid.org/0000-0002-9330-9108
Mauro Stefanon https://orcid.org/0000-0001-7768-5309

## References

Ageorges, N., Seifert, W., Jütte, M., et al. 2010, Proc. SPIE, 7735, 77351L
Asari, N. V., Cid Fernandes, R., Stasińska, G., et al. 2007, MNRAS, 381, 263
Ashby, M. L. N., Caputi, K. I., Cowley, W., et al. 2018, ApJS, 237, 39
Baldwin, J. A., Phillips, M. M., & Terlevich, R. 1981, PASP, 93, 5
Balogh, M. L., Morris, S. L., Yee, H. K. C., Carlberg, R. G., & Ellingson, E. 1999, ApJ, 527, 54
Beifiori, A., Maraston, C., Thomas, D., & Johansson, J. 2011, A&A, 531, A109
Belli, S., Genzel, R., Förster Schreiber, N. M., et al. 2017, ApJL, 841, L6
Belli, S., Newman, A. B., & Ellis, R. S. 2014, ApJ, 783, 117
Bernardi, M., Nichol, R. C., Sheth, R. K., Miller, C. J., & Brinkmann, J. 2006, AJ, 131, 1288
Bertin, G., Ciotti, L., & Del Principe, M. 2002, A&A, 386, 149
Bezanson, R., van Dokkum, P. G., Tal, T., et al. 2009, ApJ, 697, 1290
Boylan-Kolchin, M., Ma, C.-P., & Quataert, E. 2008, MNRAS, 383, 93
Brooks, A., & Christensen, C. 2016, in Galactic Bulges, ed. E. Laurikainen, R. Peletier, & D. Gadotti (Cham: Springer), 317
Bruzual, A. G. 1983, ApJS, 53, 497
Bruzual, G., & Charlot, S. 2003, MNRAS, 344, 1000
Calzetti, D., Armus, L., Bohlin, R. C., et al. 2000, ApJ, 533, 682
Cappellari, M. 2017, MNRAS, 466, 798
Cappellari, M., Bacon, R., Bureau, M., et al. 2006, MNRAS, 366, 1126
Cappellari, M., & Emsellem, E. 2004, PASP, 116, 138
Caputi, K. I., Deshmukh, S., Ashby, M. L. N., et al. 2017, ApJ, 849, 45
Cardelli, J. A., Clayton, G. C., & Mathis, J. S. 1989, ApJ, 345, 245
Cassata, P., Giavalisco, M., Williams, C. C., et al. 2013, ApJ, 775, 106
Chabrier, G. 2003, PASP, 115, 763
Cicone, C., Maiolino, R., Sturm, E., et al. 2014, A&A, 562, A21
Cid Fernandes, R., Asari, N. V., Sodré, L., et al. 2007, MNRAS, 375, L16
Cid Fernandes, R., Mateus, A., Sodré, L., Stasińska, G., & Gomes, J. M. 2005, MNRAS, 358, 363
Cimatti, A., Cassata, P., Pozzetti, L., et al. 2008, A&A, 482, 21
Ciotti, L., Lanzoni, B., & Volonteri, M. 2007, ApJ, 658, 65
Damjanov, I., Geller, M. J., Zahid, H. J., & Hwang, H. S. 2015, ApJ, 806, 158
Davidge, T. J., & Clark, C. C. 1994, AJ, 107, 946
Davies, R. I. 2007, MNRAS, 375, 1099
De Lucia, G., Springel, V., White, S. D. M., Croton, D., & Kauffmann, G. 2006, MNRAS, 366, 499
Dekel, A., & Burkert, A. 2014, MNRAS, 438, 1870
D'Eugenio, C., Daddi, E., Gobat, R., et al. 2020, ApJL, 892, L2
Estrada-Carpenter, V., Papovich, C., Momcheva, I., et al. 2020, ApJ, 898, 171
Forrest, B., Annunziatella, M., Wilson, G., et al. 2020a, ApJL, 890, L1
Forrest, B., Marsan, Z. C., Annunziatella, M., et al. 2020b, ApJ, 903, 47
Francis, P. J., Hewett, P. C., Foltz, C. B., et al. 1991, ApJ, 373, 465
Gallazzi, A., Charlot, S., Brinchmann, J., & White, S. D. M. 2006, MNRAS, 370, 1106
Gargiulo, A., Saracco, P., Longhetti, M., et al. 2015, A&A, 573, A110
Glazebrook, K., Schreiber, C., Labbé, I., et al. 2017, Natur, 544, 71
Gobat, R., Strazzullo, V., Daddi, E., et al. 2012, ApJL, 759, L44
Goto, T., Nichol, R. C., Okamura, S., et al. 2003, PASJ, 55, 771
Greggio, L., & Renzini, A. 2011, Stellar Populations. A User Guide from Low to High Redshift (Weinheim: Wiley-VCH)
Hill, A. R., Muzzin, A., Franx, M., et al. 2017, ApJ, 837, 147
Hopkins, P. F., Hernquist, L., Cox, T. J., Keres, D., & Wuyts, S. 2009, ApJ, 691, 1424
Hopkins, P. F., Murray, N., Quataert, E., & Thompson, T. A. 2010, MNRAS, 401, L19
Jeřábková, T., Hasani Zonoozi, A., Kroupa, P., et al. 2018, A&A, 620, A39
Jørgensen, I., Franx, M., & Kjaergaard, P. 1995, MNRAS, 276, 1341
Kennicutt, R. C. 1998a, ApJ, 498, 541
Kennicutt, R. C., Jr. 1998b, ARA&A, 36, 189
Kriek, M., van Dokkum, P. G., Labbé, I., et al. 2009, ApJ, 700, 221
Kriek, M., van Dokkum, P. G., Labbé, I., et al. 2018, FAST: Fitting and Assessment of Synthetic Templates, Astrophysics Source Code Library, ascl:1803.008
Kroupa, P., Subr, L., Jerabkova, T., & Wang, L. 2020, MNRAS, 498, 5652
Kubo, M., Tanaka, M., Yabe, K., et al. 2018, ApJ, 867, 1
La Barbera, F., de Carvalho, R. R., de La Rosa, I. G., et al. 2010, MNRAS, 408, 1313
La Barbera, F., Ferreras, I., Vazdekis, A., et al. 2013, MNRAS, 433, 3017
La Barbera, F., Vazdekis, A., Ferreras, I., et al. 2019, MNRAS, 489, 4090
Lanzoni, B., & Ciotti, L. 2003, A&A, 404, 819
Lapi, A., Pantoni, L., Zanisi, L., et al. 2018, ApJ, 857, 22
Magrini, L., Sommariva, V., Cresci, G., et al. 2012, MNRAS, 426, 1195
Maiolino, R., Gallerani, S., Neri, R., et al. 2012, MNRAS, 425, L66
Maiolino, R., & Mannucci, F. 2019, A&ARv, 27, 3
Maraston, C., Pforr, J., Renzini, A., et al. 2010, MNRAS, 407, 830
Maraston, C., & Strömbäck, G. 2011, MNRAS, 418, 2785
Marchesini, D., Muzzin, A., Stefanon, M., et al. 2014, ApJ, 794, 65
Marchesini, D., Whitaker, K. E., Brammer, G., et al. 2010, ApJ, 725, 1277
Marsan, Z. C., Marchesini, D., Brammer, G. B., et al. 2015, ApJ, 801, 133
Mateus, A., Sodré, L., Cid Fernandes, R., & Stasińska, G. 2007, MNRAS, 374, 1457
Mehta, V., Scarlata, C., Capak, P., et al. 2018, ApJS, 235, 36
Miller, N. A., & Owen, F. N. 2002, AJ, 124, 2453
Moustakas, J., Kennicutt, R. C., Jr, & Zaritsky, D. 2005, AAS Meeting, 207, 43.02
Muzzin, A., Marchesini, D., Stefanon, M., et al. 2013, ApJS, 206, 8
Naab, T., Johansson, P. H., & Ostriker, J. P. 2009, ApJL, 699, L178
Naab, T., Johansson, P. H., Ostriker, J. P., & Efstathiou, G. 2007, ApJ, 658, 710
Newman, A. B., Belli, S., Ellis, R. S., & Patel, S. G. 2018, ApJ, 862, 126
Nipoti, C., Treu, T., Auger, M. W., & Bolton, A. S. 2009, ApJL, 706, L86
Nipoti, C., Treu, T., Leauthaud, A., et al. 2012, MNRAS, 422, 1714
Oser, L., Naab, T., Ostriker, J. P., & Johansson, P. H. 2012, ApJ, 744, 63
Oser, L., Ostriker, J. P., Naab, T., Johansson, P. H., & Burkert, A. 2010, ApJ, 725, 2312
Pantoni, L., Lapi, A., Massardi, M., Goswami, S., & Danese, L. 2019, ApJ, 880, 129
Peng, Y., Maiolino, R., & Cochrane, R. 2015, Natur, 521, 192
Pietrinferni, A., Cassisi, S., Salaris, M., & Castelli, F. 2004, ApJ, 612, 168
Poggianti, B. M., & Barbaro, G. 1997, A&A, 325, 1025
Renzini, A. 2006, ARA&A, 44, 141
Salpeter, E. E. 1955, ApJ, 121, 161
Saracco, P., Gargiulo, A., La Barbera, F., Annunziatella, M., & Marchesini, D. 2020, MNRAS, 491, 1777
Saracco, P., La Barbera, F., Gargiulo, A., et al. 2019, MNRAS, 484, 2281
Saracco, P., Longhetti, M., & Andreon, S. 2009, MNRAS, 392, 718
Saracco, P., Longhetti, M., & Gargiulo, A. 2011, MNRAS, 412, 2707
Saulder, C., van den Bosch, R. C. E., & Mieske, S. 2015, A&A, 578, A134
Schreiber, C., Glazebrook, K., Nanayakkara, T., et al. 2018, A&A, 618, A85
Scodeggio, M., Franzetti, P., Garilli, B., et al. 2005, PASP, 117, 1284
Serven, J., Worthey, G., & Briley, M. M. 2005, ApJ, 627, 754
Silverman, J. D., Lamareille, F., Maier, C., et al. 2009, ApJ, 696, 396
Springel, V., Pakmor, R., Pillepich, A., et al. 2018, MNRAS, 475, 676
Straatman, C. M. S., Labbé, I., Spitler, L. R., et al. 2014, ApJL, 783, L14
Tacchella, S., Dekel, A., Carollo, C. M., et al. 2016, MNRAS, 458, 242
Tanaka, M., Hasinger, G., Silverman, J. D., et al. 2017, arXiv:1706.00566
Tanaka, M., Valentino, F., Toft, S., et al. 2019, ApJL, 885, L34
Tanaka, M., Valentino, F., Toft, S., et al. 2020, ApJL, 894, L13
Thomas, D., Maraston, C., Schawinski, K., Sarzi, M., & Silk, J. 2010, MNRAS, 404, 1775
Trager, S. C., Faber, S. M., Worthey, G., & González, J. J. 2000, AJ, 120, 165
Trager, S. C., Worthey, G., Faber, S. M., Burstein, D., & González, J. J. 1998, ApJS, 116, 1
Valdes, F., Gupta, R., Rose, J. A., Singh, H. P., & Bell, D. J. 2004, ApJS, 152, 251
Valentino, F., Tanaka, M., Davidzon, I., et al. 2020, ApJ, 889, 93
Valentinuzzi, T., Fritz, J., Poggianti, B. M., et al. 2010, ApJ, 712, 226
van de Sande, J., Kriek, M., Franx, M., et al. 2013, ApJ, 771, 85
Vazdekis, A., Casuso, E., Peletier, R. F., & Beckman, J. E. 1996, ApJS, 106, 307
Vazdekis, A., Coelho, P., Cassisi, S., et al. 2015, MNRAS, 449, 1177
Wellons, S., Torrey, P., Ma, C.-P., et al. 2015, MNRAS, 449, 361
Woo, J., Dekel, A., Faber, S. M., & Koo, D. C. 2015, MNRAS, 448, 237
Worthey, G., Faber, S. M., & Gonzalez, J. J. 1992, ApJ, 398, 69
Worthey, G., & Ottaviani, D. L. 1997, ApJS, 111, 377
Yan, Z., Jerabkova, T., & Kroupa, P. 2019, A&A, 632, A110